ADVANCED HEALTHCARE MATERIALS
www.advhealthmat.de

Manganese-Based Biofunctional 2D Nanosheets Enabled In Situ Macrophage Engineering for Precise Eradication of Osteomyelitis

Shengchang Zhang, Huaijuan Zhou, Bowen Chi, Zdenek Sofer, Paul K. Chu,* Yilong Wang, and Jinhua Li**

Efficient treatment of osteomyelitis caused by *Staphylococcus aureus* is a great clinical challenge due to bacterial resistance and immune evasion issues. Macrophages play a crucial role in the fight against *S. aureus* but suffer from deficiencies in function in the infectious milieu leading to persistent infection. Here, a strategy of exploiting aged neutrophil membrane (aNM) is developed to camouflage 2D $MnPSe_3$ nanosheets (MPS NSs), denoted as aNM@MPS, to mediate in situ macrophage engineering, thereby potentiating macrophages to eradicate refractory osteomyelitis. When administered systematically, the biofunctional aNM@MPS ensures selectivity for osteomyelitis lesions, enhanced bone marrow retention, and subsequent phagocytosis by macrophages. In the mouse model of osteomyelitis, the aNM@MPS enables dysfunctional macrophages to digest intracellular bacteria by generating highly toxic hydroxyl radicals and sequentially reprogramming bactericidal immunity through manganese ion-mediated immune activation, which synergistically terminates persistent infection-initiated pathological cascades and subsequently reestablish host-directed bactericidal potency, thereby conferring a satisfactory osteoprotective effect. These findings demonstrate that macrophages in the skeletal infectious milieu can be precisely remodeled via the lesion–macrophage dual-targeting metalloimmunotherapy strategy, which holds potential for osteomyelitis treatment.

1. Introduction

Osteomyelitis, a particularly devastating complication following orthopedic surgery or bacteremia, remains a significant clinical challenge.[1] The management of osteomyelitis necessitates complex treatment strategies, including prolonged antibiotic therapy and extensive surgical debridement.[2] However, limited clinical progress has been made in terms of eradicating osteomyelitis due to bacterial persistence. Among the diverse pathogens linked to osteomyelitis, *Staphylococcus aureus*, particularly methicillin-resistant *S. aureus* (MRSA), represents the most prevalent and destructive causative agent regarding osteomyelitis.[1a,3] Because osteomyelitis-causing *S. aureus* can cause host immune paralysis and evade antibiotic chemotherapy,[4] restimulating bactericidal immunity in the skeletal infectious microenvironment is critical in eradicating osteomyelitis. However, effective treatment strategies remain largely unexplored.

Macrophages play a pivotal role in orchestrating the bactericidal immune response to *S. aureus*, which mainly relies on a burst of reactive oxygen species (ROS) after internalizing the pathogens and serially

S. Zhang, J. Li
School of Medical Technology
Beijing Institute of Technology
Beijing 100081, China
E-mail: lijinhua@bit.edu.cn
H. Zhou
School of Interdisciplinary Science
Beijing Institute of Technology
Beijing 100081, China
E-mail: huaijuan.zhou@bit.edu.cn
B. Chi, Y. Wang
Department of Neurology
Beijing Tiantan Hospital
Capital Medical University
Beijing 100070, China
Z. Sofer
Department of Inorganic Chemistry
University of Chemistry and Technology Prague
Technicka 5, 166 28 Prague 6, Czech Republic
P. K. Chu
Department of Physics
Department of Materials Science and Engineering
and Department of Biomedical Engineering
City University of Hong Kong
Tat Chee Avenue, Kowloon, Hong Kong 999077, China
E-mail: paul.chu@cityu.edu.hk
The ORCID identification number(s) for the author(s) of this article can be found under https://doi.org/10.1002/adhm.202500169

DOI: 10.1002/adhm.202500169

initiating adaptive immunity via antigen presentation.[5] However, postoperative local tissue response and progressive infections lead to a niche of immune paralysis that impairs the phagocytic and bactericidal activities of macrophages.[4b,6] Furthermore, *S. aureus*-infected macrophages with inadequate ROS levels weaken phagolysosomal killing, thus permitting the intracellular survival of pathogens and allowing for persistent infection.[7] As macrophages possess unique effector functions in terms of host defense against pathogens,[8] it is hypothesized that the in situ targeted reprogramming of the macrophages in the skeletal infectious microenvironment to restore immune defense could redirect the phagocytosis and reinforce the phagolysosomal killing activity of staphylococcus-infected macrophages, thereby thwarting bacterial immune evasion via a host-directed strategy and subsequently eradicating uncontrolled osteomyelitis.

The precise targeting of macrophages in the skeletal infectious microenvironment is crucial in efficiently remodeling macrophage-initiated bactericidal immune cascades. Aged neutrophils (aNEs) can home to bone marrow for safe removal, which is a critical innate function on the part of neutrophils to help maintain tissue homeostasis.[9] During the homing of aNEs to the bone marrow, the overexpression of the chemokine receptor CXCR4 on the aNEs' plasma membrane is a key signal to connect with the CXC chemokine ligand 12 (CXCL12) in the bone marrow, which guides aNE homing.[10] Critically, when aNEs migrate back into the bone marrow, macrophages prefer to recognize and phagocytose them there.[9b,11] Inspired by this, the camouflage with aged neutrophil membrane (aNM) may therefore enhance the bone marrow homing of nanoformulations and serially enable the specific internalization of macrophages. Importantly, nanoformulation-armed infected macrophages elicit a highly reactive ROS burst within the phagosome, which is crucial in effectively eliminating intracellular pathogens. Typically, ROS-catalytic metal-based enzymatic nanoformulations exhibit robust Fenton/Fenton-like reactions that produce highly toxic hydroxyl radicals (•OH).[12] Moreover, metal ions, especially manganese ions, are effective immunologic adjuvants for metalloimmunotherapies.[13] Superior to the free ion state, 2D ternary manganese-based layered materials, such as $MnPSe_3$ and $MnPS_3$, are emerging biomaterials due to their inherent enzyme mimetics and potential immunostimulatory properties.[14] However, biological barriers and non-specific distribution remain formidable challenges for 2D layered material-based precision therapeutics.[15] As such, aNM-coated 2D ternary manganese-based enzymatic nanoformulations may be an efficient way to manipulate macrophages in skeletal infectious microenvironment in situ such that they digest intracellular multidrug-resistant bacteria and restimulate innate anti-bacterial immunity, which can enable the host-directed bactericidal strategy and thus eradicate osteomyelitis.

Here, we sought to develop biofunctional nanosheets for infected bone marrow homing and the in situ reprogramming of microenvironmental macrophages to enable the precise eradication of osteomyelitis. 2D $MnPSe_3$ nanosheets (MPS NSs), incorporating divalent manganese, phosphorus, and selenium ions, are a promising candidate for immunostimulation and osteoprotection. Such metalloimmunotherapy based on aNM-cloaked MPS NSs possesses both the improved accumulation in the lesional bone marrow and the ability to remodel macrophage-initiated bactericidal immune cascades, thereby reversing uncontrolled osteomyelitis (**Figure 1**). With the shielding of aNM, the obtained aNM@MPS is endowed with stealth properties in the circulation and can realize the bone marrow homing, thus enhancing the retention in osteomyelitic lesions. When aNM@MPS is enriched in the lesional bone marrow, the biofunctional nanosheets are subsequently phagocytosed by macrophages. These aNM@MPS-armed dysfunctional macrophages have demonstrated the capabilities to digest intracellular bacteria by generating highly toxic •OH, serially reconstruct anti-bacteria host immunity, and ultimately confer an osteoprotective effect.

2. Results

2.1. Preparation and Characterization of aNM@MPS

To obtain aNM, neutrophils with an average purity of 96.5% (Figure S1, Supporting Information) were isolated from mouse bone marrow and cultured in vitro for aging. Aged neutrophils up-regulate CXCR4 expression, causing them to migrate to the bone marrow for their natural removal.[9a] Given the half-life of neutrophils,[16] those that had been aged for 8 h and exhibited high CXCR4 expression levels (Figure S2, Supporting Information) were selected for the preparation of aNM. Next, MPS NSs were prepared via the liquid-phase exfoliation of bulk $MnPSe_3$ powder in an aqueous solution using sonication. The transmission electron microscopy (TEM) image of the bulk $MnPSe_3$ shows a tightly packed, laminated microstructure (**Figure 2a**). The TEM image also shows that the exfoliated MPS NSs in the above bulk $MnPSe_3$ have a typical sheet-like morphology (Figure 2b), with a hydrodynamic size of ≈190 nm (Figure 2d). Additionally, the Raman spectrum of bulk $MnPSe_3$ and MPS NSs, as shown in Figure S3 (Supporting Information), displays representative Raman modes, which are consistent with previous reports.[17] Subsequently, the aNM was coated on the MPS NSs via sonication. Figure 2c shows a TEM image of aNM@MPS, which reveals a typical sheet-like core–shell structure like that of bare MPS NSs. The increased diameter further indicates the successful coating of the aNM (≈10 nm in thickness) on the surface of the MPS NSs (Figure 2d). For visualization, the red dye Rhodamine B (RhB) and green dye 5(6)-Carboxyfluorescein diacetate succinimidyl ester (CFSE) were loaded into the MPS NSs and aNM, respectively. The colocalization of both fluorescence signals indicated the successful association of the two components (Figure 2e). Next, we examined the expression of CXCR4 in the aNM@MPS. Sodium dodecyl sulfate-polyacrylamide gel electrophoresis revealed the preservation of similar protein profiles in aNM@MPS (Figure S4, Supporting Information). Importantly, flow cytometry analysis showed that the aNM@MPS possesses CXCR4, a critical protein marker of senescent neutrophils, after successful membrane cloaking (Figure 2f). Collectively, these results demonstrated successful aNM coating.

The migration of aNEs to the bone marrow is guided by the CXCR4/CXCL12 signaling axis.[10a] Thus, a transwell-based model was designed via which to evaluate the responsiveness of the aNM@MPS to CXCL12 (Figure 2g, left). The statistical analysis suggested that the CXCL12-treated aNM@MPS group exhib-

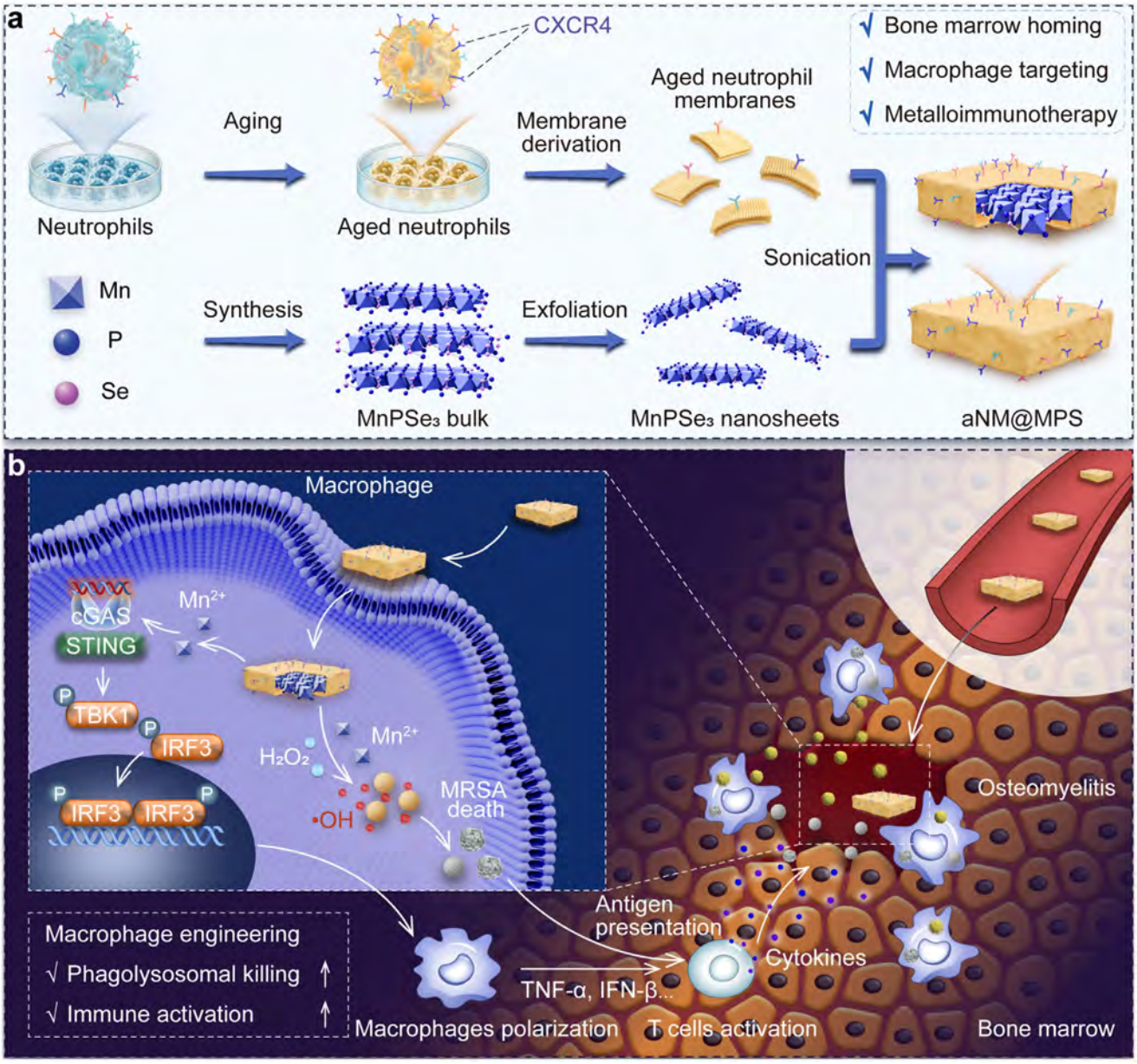

Figure 1. Schematic of the preparation process and anti-osteomyelitis mechanism of aNM@MPS. a) Preparation of aNM@MPS. b) After intravenous injection and accumulation in osteomyelitis lesions, aNM@MPS can effectively arm macrophages to kill intracellular bacteria, sequentially eliciting host-directed bactericidal immune cascades, thereby conferring an osteoprotective effect. TBK1, TANK-binding kinase 1; IRF3, interferon regulatory factor 3.

ited a much higher fluorescence intensity (Figure 2g, right), implying that the biofunctional nanosheets engage in bone marrow homing. In addition, manganese ions-based enzymatic nanoformulations exhibited sensitive catalytic activity that converted less-toxic H_2O_2 into highly toxic •OH, effectively enhancing oxidative damage.[18] Thus, we used terephthalic acid to determine the level of •OH generation. The introduction of aNM@MPS into the mimicking lysosomal environment successfully elevated the levels of •OH, thereby significantly facilitating the oxidation of terephthalic acid to yield the fluorescent product 2-hydroxyterephthalic acid (Figure 2h). These results demonstrated the aNM@MPS provides enhanced chemodynamic activity against bacteria, enabling the efficient induction of phagolysosomal killing.

2.2. Enhancement of Bactericidal Activity by aNM@MPS-Armed Macrophages In Vitro

Aged neutrophils are preferred in terms of being recognized and phagocytosed by macrophages.[9b,11a] We investigated the engulfment of the aNM cloaking nanosheets in vitro using bone

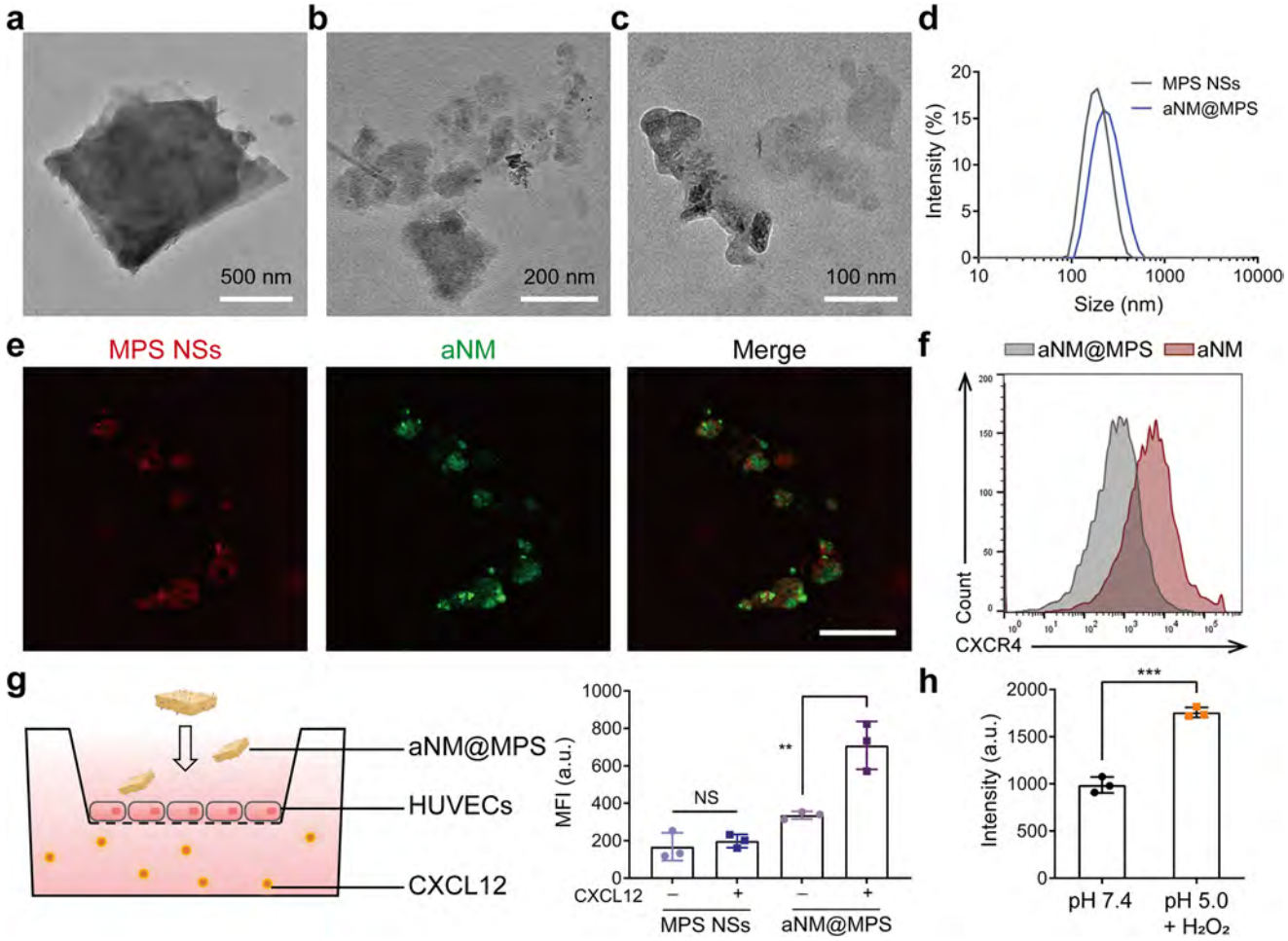

Figure 2. Preparation and characterization of aNM@MPS. a) Representative TEM images of bulk $MnPSe_3$ ($n = 3$ independent experiments). Scale bar, 500 nm. b) Representative TEM image of the exfoliated MPS NSs ($n = 3$ independent experiments). Scale bar, 100 nm. c) Representative TEM image of aNM@MPS ($n = 3$ independent experiments). Scale bar, 100 nm. d) The hydrodynamic diameters of various nanosheets measured by dynamic light scattering ($n = 3$ independent experiments). e) Fluorescence images of aNM@MPS. Red: RhB-labeled MPS NSs; Green: CFSE-labeled aNM ($n = 3$ independent experiments). Scale bar, 10 μm. f) Flow cytometry analysis of the presence of CXCR4 on the surface of aNM@MPS ($n = 3$ independent experiments). g) Schematic of the transwell migration model (lift) and the quantitative result of migratory aNM@MPS with or without CXCL12 (right). The results are reported as the mean ± s.d. ($n = 3$ independent experiments). MFI, mean fluorescence intensity; a.u., arbitrary units. h) Detection of •OH generated by aNM@MPS. Nonfluorescent terephthalic acid was converted to fluorescent 2-hydroxyterephthalic acid by •OH oxidation. The results are reported as the mean ± s.d. ($n = 3$ independent experiments). Statistical significance was determined by a two-sided Student's t test in (g) and (h). $^{**}P < 0.01$, $^{***}P < 0.001$. NS, not significant.

marrow-derived macrophages (BMDMs; Figure S5, Supporting Information). As shown in **Figure 3**a, substantial enhancement was achieved regarding the in vitro cellular internalization of aNM@MPS after the nanosheet was coated in aNM. In contrast, a minimal red signal was detected in the uncoated MPS NSs treatment group. The result was further confirmed with flow cytometry, indicating that the aNM@MPS was efficiently delivered into the macrophages (Figure 3b). We then investigated the intracellular trafficking of the biofunctional nanosheets. Confocal laser scanning microscopy (CLSM) images indicate that aNM@MPS was localized specifically with the endo/lysosomes of macrophages (Figure 3c). The Pearson correlation coefficient of the colocalization of Lyso Tracker Green DND-26-labeled lysosomes (green) with RhB-labeled aNM@MPS (red) further confirmed the above observation (Figure 3d). In addition, the cell-counting kit-8 (CCK8) assay results revealed that the biofunctional nanosheets had excellent cell safety (Figure S6, Supporting Information). Together, our findings indicate that aNM@MPS have the potential for biomedical applications related to macrophage-targeted delivery.

Infected macrophages failed to eradicate intracellular infections.[19] To test whether the specific cellular internalization of aNM@MPS would be beneficial for intracellular infection clearance, we examined the intracellular killing of MRSA by various treatment groups of BMDMs. In view of the fact that the toxic ROS had limited effective radii of action (less than 200 nm),[20] we intended to ascertain whether the biofunctional nanosheets would colocalize with intracellular bacteria after being efficiently taken up by macrophages. As demonstrated in Figure 3e, the RhB-labeled aNM@MPS matched with the

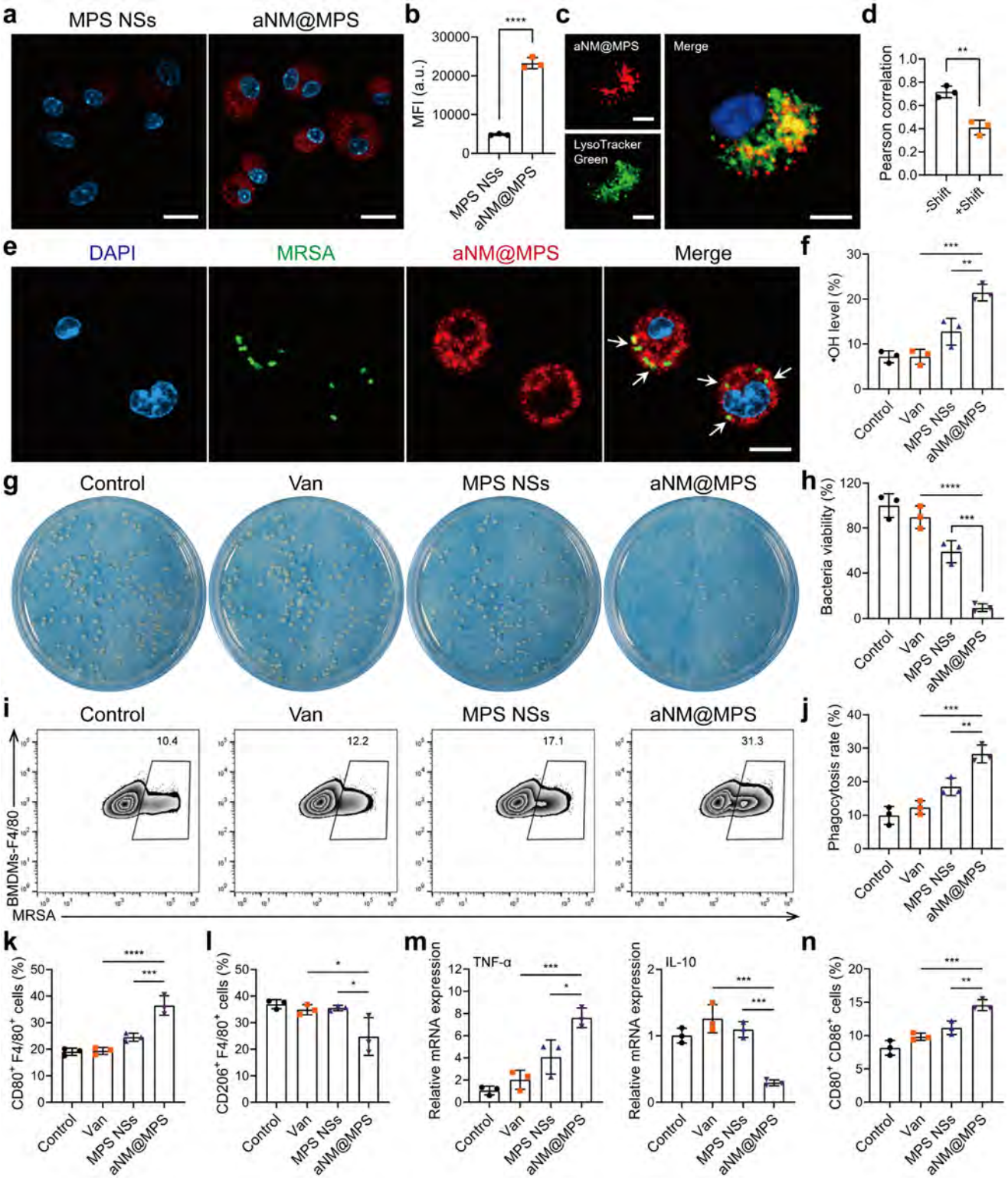

Figure 3. Macrophage targeting and bactericidal activity of aNM@MPS in vitro. a) Fluorescence images of BMDMs treated with uncoated MPS NSs or aNM@MPS ($n = 3$ independent experiments). The nuclei were counterstained with DAPI (blue). Scale bars, 20 μm. b) Cellular uptake of uncoated MPS NSs or aNM@MPS by BMDMs as measured through flow cytometry analysis. The results are reported as the mean ± s.d. ($n = 3$ independent experiments). c,d) Representative images (c) and Pearson correlation (d) of colocalization of LysoTracker-labeled lysosomes (green) with RhB-labeled aNM@MPS (red). The nuclei were counterstained with DAPI (blue). Pearson correlation with (+) and without (−) a 20-pixel shift (the approximate lysosome diameter) of the green signal. The results are reported as the mean ± s.d. ($n = 3$ cells per group). Scale bar, 10 μm. e) Confocal images of in-

CFSE-labeled MRSA well, implying the selectively bactericidal ability of aNM@MPS regarding phagosomal bacteria. Because of the ability of aNM@MPS to efficiently catalyze •OH generation, we investigated its intracellular catalytic activity by monitoring •OH levels. Consistently, we found that aNM@MPS-treated infected macrophages exhibited noticeable •OH generation (Figure 3f; Figure S7, Supporting Information). Next, we evaluated the phagolysosomal killing ability of NM@MPS-treated macrophages. BMDMs were infected with MRSA and then treated with aNM@MPS, MPS NSs, vancomycin (Van), and phosphate-buffered saline (PBS) (control group). Among these treatments, the aNM@MPS group showed the strongest bactericidal activity, with 90.52% inhibition (Figure 3g,h). This can be attributed to the remarkable cellular internalization of the biofunctional nanosheets and their effective catalytic activity in terms of generating •OH for oxidative killing. Notably, the biofunctional nanosheets reestablished the pathogen phagocytosis ability of infected macrophages. As shown in the confocal microscopy images presented in Figure S8 (Supporting Information), the aNM@MPS-armed macrophages led to their robust phagocytosis of MRSA. Consistently, the proportion of armed macrophages that phagocytized MRSA in the aNM@MPS treatment group was 2.9 times higher than that in the control group (Figure 3i,j).

Persistent bacterial infections often induce an immunosuppressive M2-like macrophage phenotype that fosters bacterial growth and attenuates antibacterial therapy.[21] Proinflammatory macrophages are thought to demonstrate significant phagocytic and bactericidal activity against bacteria and sequentially trigger acquired immune responses.[22] To further elucidate the mechanisms that underlie the efficacy of biofunctional nanosheets in enhancing macrophages' phagocytic and bactericidal activity, we next performed a phenotype analysis of macrophages after aNM@MPS treatment. As shown in Figure 3k,l, and Figure S9 (Supporting Information), the percentage of $CD80^+$ M1-phenotype cells was increased significantly in the aNM@MPS group as compared to the other groups, whereas the percentage of $CD206^+$ M2-phenotype cells was decreased significantly. We further validated the induction of a proinflammatory M1 phenotype using quantitative reverse transcription polymerase chain reaction (qRT-PCR), which demonstrated similar results, such as the increased expression of the M1 biomarker tumor necrosis factor-α (TNF-α) and the reduced expression of the M2 biomarker IL-10 in aNM@MPS-treated macrophages (Figure 3m). In addition, the gene expression of the type I interferon (IFN) biomarker of IFN-β was effectively elevated in cells treated with aNM@MPS (Figure S10, Supporting Information), which is additional evidence for the activation of proinflammatory macrophages, as IFN-β is the key downstream protein of cyclic guanosine monophosphate-adenosine monophosphate synthase (cGAS)–stimulator of interferon genes (STING) pathway activation. To verify the formation of in situ STING activation, we examined the relative gene expression of the cGAS-STING axis and the phosphorylation levels of associated proteins in macrophages after various treatments using qRT-PCR analysis and western blot, respectively. As indicated, aNM@MPS-treated macrophages exhibited a significant increase in the relative expression of cGAS-STING axis genes of cGAS, STING, and CXCL10 (Figure S10b–d, Supporting Information). Notably, aNM@MPS significantly augmented the phosphorylation levels of TBK1 and IRF3, proving that aNM@MPS treatment effectively activated cGAS-STING signal transduction in macrophages (Figure S10e, Supporting Information). These results indicated that aNM@MPS-mediated macrophages' reprogramming could enhance their polarization into the proinflammatory M1 phenotype, which confirmed that biofunctional nanosheets would specifically boost the phagocytic and bactericidal activity of macrophages. In addition, we found that the proportion of $CD80^+CD86^+$ macrophages was upregulated after M2-like BMDMs were pretreated with aNM@MPS (Figure 3n; Figure S11, Supporting Information). The overexpressed co-stimulators contribute to antigen presentation and sequentially activate MRSA-specific T cell responses. In total, aNM@MPS treatment was beneficial in terms of reinvigorating macrophages' phagocytic and bactericidal activity, thereby restimulating host immunity.

2.3. Bone Marrow Localization of the Biofunctional Nanosheets In Vivo

An implant-related osteomyelitis mouse model was first established as previously reported.[23] We next investigated the in vivo biodistribution and bone marrow targeting properties of aNM@MPS. The major organs and hindlimb long bones of the osteomyelitis mice from each group were collected at 8 and 24 h post intravenous administration and subjected to fluorescence analysis ex vivo. As shown in **Figure** 4a,b, aNM@MPS was superior to MPS NSs in terms of intra-bone accumulation, indicating the specific bone marrow targeting property of the biofunctional nanosheets. In addition, although the nanosheets from both groups were highly distributed in the liver and spleen after tail vein injection, the aNM@MPS group exhibited faster clearance from these organs as compared to the MPS NSs group (Figure 4a,c). At the study endpoint, the bone tissue profile also demonstrated that aNM@MPS was preferen-

tracellular CFSE-MRSA (green) after incubation with aNM@MPS (red). White arrows indicate the colocalization of MRSA (green pixels) with aNM@MPS (red pixels) ($n = 3$ independent experiments). Scale bars, 20 µm. f) Quantitation of •OH in BMDMs with hydroxyphenyl fluorescein. The results are reported as the mean ± s.d. ($n = 3$ independent experiments). g,h) Representative images g) and quantitative analysis h) of the intracellular survival of MRSA in BMDMs (multiplicity of infection = 5:1) in the indicated treatment groups. The results are reported as the mean ± s.d. ($n = 3$ independent experiments). i) Flow cytometry detected the phagocytosis of labeled MRSA by BMDMs treated with the different formulations ($n = 3$ independent experiments). j) Statistical analysis of the MRSA phagocytosis index in Figure (i). The results are reported as the mean ± s.d. ($n = 3$ independent experiments). k,l) The proportions of proinflammatory ($F4/80^+CD80^+$) (k) and anti-inflammatory ($F4/80^+CD206^+$) (l) macrophage in each treatment group according to flow cytometry analysis. The results are reported as the mean ± s.d. ($n = 3$ independent experiments). m) Gene expression of TNF-α and IL-10. The results are reported as the mean ± s.d. ($n = 3$ independent experiments). n) The proportion of $CD80^+CD86^+$ BMDMs after treatment with different nanoformulations. The results are reported as the mean ± s.d. ($n = 3$ independent experiments). Statistical significance was determined by a two-sided Student's t test in (b) and (d) and one-way ANOVA with Tukey's post hoc test for (f), (h), (j), (k–n). $^*P < 0.05$, $^{**}P < 0.01$, $^{***}P < 0.001$, $^{****}P < 0.0001$.

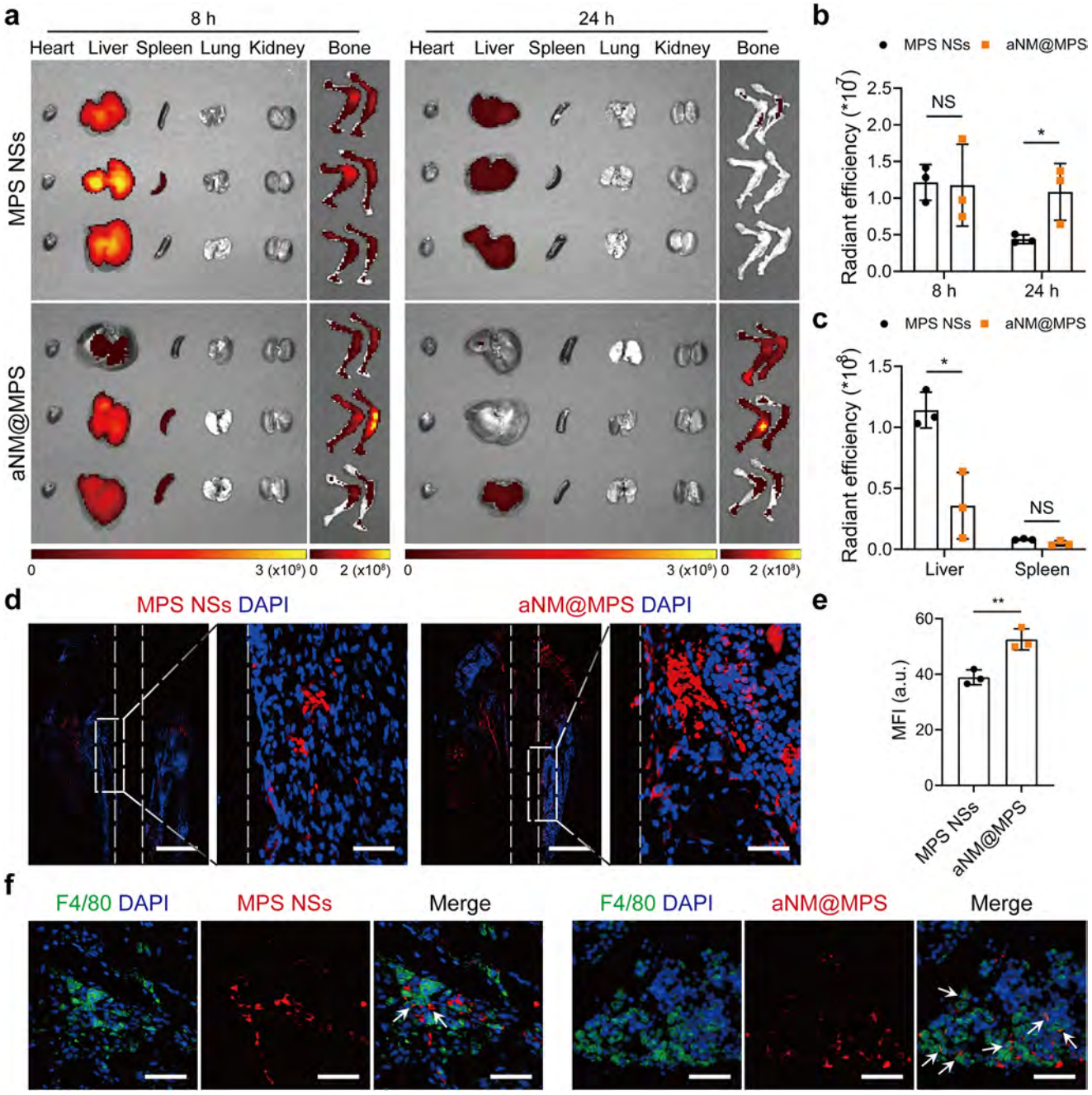

Figure 4. Accumulation of aNM@MPS in bone marrow. a) Fluorescence images of excised major organs and hind limb long bone that were collected from mice receiving RhB-labeled aNM@MPS or MPS NSs at 8 and 24 h after administration and were captured using an IVIS Spectrum Imaging System with λex/λem = 748/780 nm ($n = 3$ biologically independent animals per group). b,c) Quantification of fluorescence intensity in the hind limb long bone (b) and spleen and liver (c) of osteomyelitis mice. Data are the mean ± s.d. ($n = 3$ biologically independent animals per group). d) Trafficking profile of the biofunctional nanosheets in the bone marrow. Red represents nanosheets and blue represents nuclei. Scale bars, 500 and 50 µm. e) Quantitative analysis of the accumulation of the nanosheets in the bone marrow of the treated mice. Data are presented as the mean ± s.d. ($n = 3$ independent experiments). f) Representative images of the biofunctional nanosheets engulfed by macrophages in vivo. Blue, DAPI-stained cell nuclei; Red, RhB-labeled nanosheets; Green, FITC-conjugated anti-F4/80 antibodies-labeled macrophages. The arrow indicates the colocalization of the nanosheets and macrophages labeled with anti-F4/80 antibodies ($n = 3$ independent experiments). Scale bars, 50 µm. Statistical significance was determined by a two-sided Student's t test in (b), (c), and (e). $^*P < 0.05$, $^{**}P < 0.01$. NS, not significant.

tially enriched in the bone marrow as compared to the bare nanosheet-treated group (Figure 4d,e). Further immunofluorescence staining demonstrated that aNM@MPS colocalized with the macrophages well (Figure 4f), confirming that the biofunctional nanosheets could efficiently home to bone marrow and specifically target macrophages in situ.

The systemic safety of the intravenously administered biofunctional nanosheets was also tested. In a titanium-based bone-implanted mouse model, throughout the study period of up to 4 weeks, blood biochemical parameters and routine blood parameters of the aNM@MPS-treated mice did not exhibit any statistically significant differences compared to those of the PBS control group (Figure S12a,b, Supporting Information). The histological analyses (Figure S12c, Supporting Information) of the organs of mice treated with aNM@MPS yielded results comparable to those of animals that were treated with PBS, lacking marked signs of systemic toxicity. Similarly, the pathological section of the peri-implant bone tissue also showed no significant changes in cell apoptosis or inflammatory cell infiltration (Figure S12d, Supporting Information). Together, these results suggest that our biofunctional nanosheets have excellent biocompatibility.

2.4. Anti-Infection and Immunity Activation Effects of aNM@MPS In Vivo

Given the potent aNM@MPS-mediated bactericidal activity observed in vitro, we next tested the bactericidal effects of the biofunctional nanosheets in an in situ implant-related osteomyelitis mouse model (**Figure 5a**). At the study endpoint, the colony counting results from the bone marrow aspirates showed that the numbers of both intracellular and extracellular MRSA colonies in the aNM@MPS-treated group were significantly lower than those in the control, Van, or MPS-NS-treated groups (Figure 5b,c; Figure S13a,b, Supporting Information). In addition, hematoxylin and eosin (H&E) staining showed that the peri-implant bone tissue exhibited an almost normal structure in the aNM@MPS group, whereas the typical abscess formation was observed in the other treatment groups, indicating persistent osteomyelitis (Figure 5d). Gram staining was used to investigate the residual bacteria in the bone tissue surrounding the implant. As shown in Figure 5e (blue arrows), in comparison to the aNM@MPS group, numerous bacteria are found in Gram-stained sections taken from the control, Van, and MPS NS groups. The scanning electron microscopy (SEM) images of extracted implants showed consistent results. aNM@MPS eliminated the majority of bacteria on the implant and thus destroyed the formation of biofilms (Figure S14a, Supporting Information). In contrast, numerous bacteria occupied the surface of implants that were harvested from control, Van, and MPS NSs groups. Besides, optical images of bacterial colonies obtained by rolling the implant on agar plates revealed that a minimal number of bacteria were observed on the implant surface in mice treated with aNM@MPS (Figure S14b, Supporting Information). Therefore, these results suggest an excellent anti-infection effect on the part of the biofunctional nanosheets on in situ implant-related osteomyelitis.

To elucidate whether aNM@MPS contributes to an effective antimicrobial immunologic response, we first analyzed the proportion of myeloid-derived suppressor cells (MDSCs) around the infected region on day 14 after infection. MDSCs have a pivotal function in orchestrating the immunosuppressive microenvironment in implant-related bone infections.[21a] The percentage of $CD11b^+Gr\text{-}1^+$ MDSCs in the aNM@MPS treatment group was far less than those in the control, Van, and MPS NS groups (Figure 5f,g), which coincided with a lower bacterial burden, implying the reverse of an immunosuppressive niche. Considering the fact that MDSC infiltration is a negative regulator of macrophage function, we explored whether a change in MDSCs affects the phenotype of macrophages in infected tissue. As expected, treatment with aNM@MPS did induce phenotypic alterations in infected macrophages. The quantitative flow cytometry results showed that the population of M1-phenotype macrophages in the infected region in the aNM@MPS treatment group was much higher than that in the other groups (Figure 5h; Figure S15a, Supporting Information); the opposite trend was observed for the anti-inflammatory phenotype of the macrophages (Figure 5i; Figure S15a, Supporting Information). Because the M1-phenotype shift regarding the macrophages may highlight the possibility of adaptive immunity activation, we next analyzed T-cell infiltration in the peri-implant bone tissue. Compared with the other groups, the significant infiltration of $CD4^+/CD8^+$ T-cells was found in the aNM@MPS treatment group (Figure 5j,k; Figure S15b, Supporting Information); these are vitally important in reestablishing host-directed bactericidal immunity. The above results collectively suggest that the administration of biofunctional nanosheets reversed the infection-induced immunocompromised milieu, thereby conferring vigorous bactericidal immune activity and eradicating uncontrolled osteomyelitis.

Persistent infection in osteomyelitis typically leads to progressive bone destruction.[2a] We wished to ascertain whether the biofunctional nanosheet treatment would have an osteoprotective effect. Thus, we performed immunofluorescence staining to characterize the expression of osteocalcin (OCN), a crucial late osteogenic marker. In alignment with the observed therapeutic efficacy against infection, immunofluorescence imaging revealed a significant enhancement in OCN secretion within the peri-implant bone tissue of the aNM@MPS-treated groups as compared to the other groups (Figure 5l,m). The above-mentioned in vivo results unequivocally demonstrate the potential of these functional nanosheets to effectively eliminate MRSA infections and promote sequential osteoprotection.

2.5. Anti-Hematogenous Osteomyelitis Effects of aNM@MPS In Vivo

Osteomyelitis can arise due to hematogenous dissemination from systemic bacteremia, potentially occurring at any time in previously healthy implant or bone tissue, leading to an uncontrolled infection.[24] Thus, we established a MRSA-induced hematogenous implant-related osteomyelitis mouse model to evaluate the potential clinical application of the biofunctional nanosheets (**Figure 6a**). At the study endpoint, the aNM@MPS-treated group exhibited the lowest extracellular and intracellular bacterial burdens among all groups (Figure 6b; Figure S16, Supporting Information), which was attributed to its exceptional bone marrow homing capability for the osteomyelitis site and se-

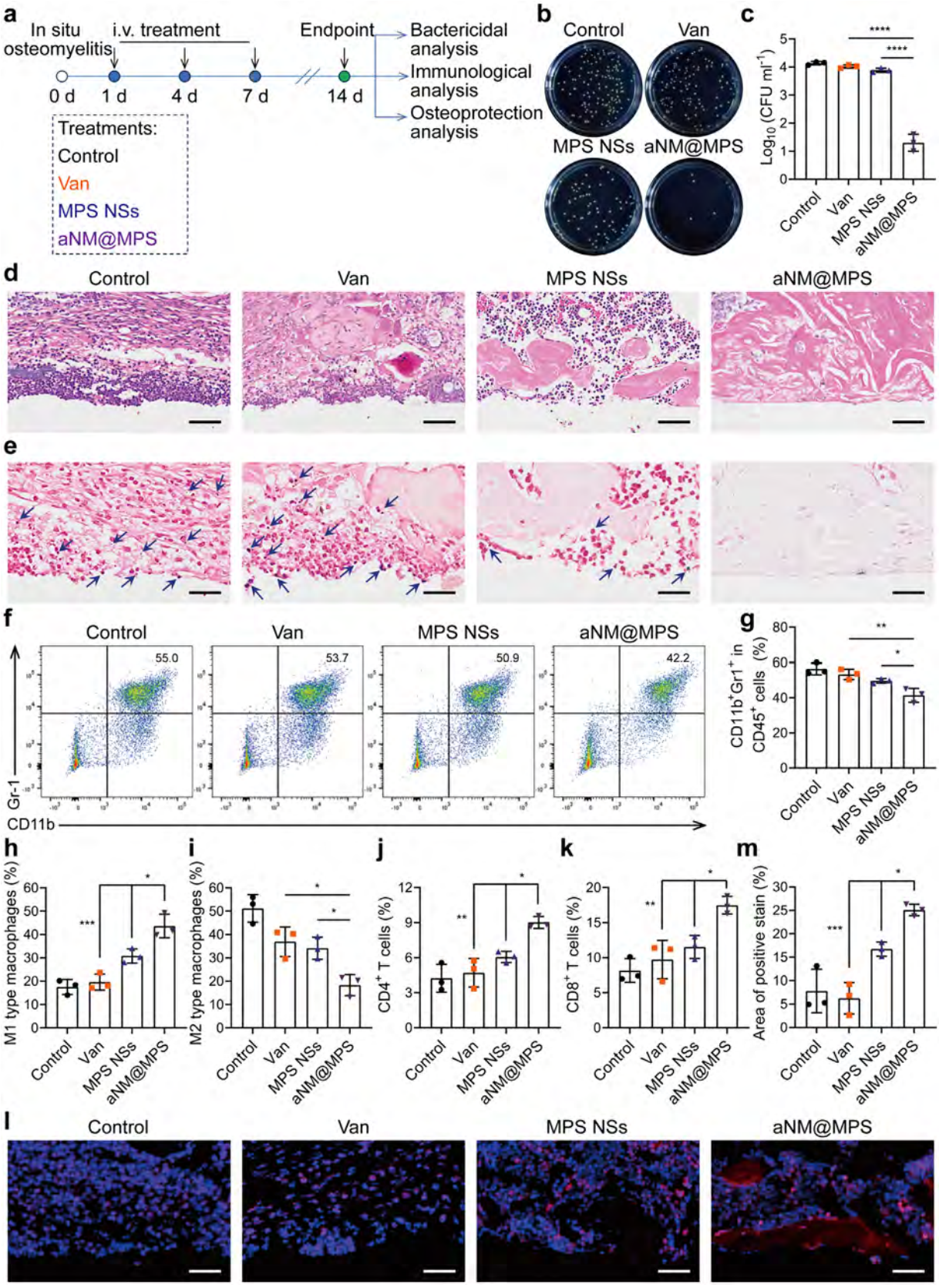

rially induced macrophage-mediated robust bactericidal immunity. An important pathogenesis in *S. aureus*-induced osteomyelitis is the formation of biofilms.[25] Invading bacteria prefer to colonize the implant, and thus, they lead to persistent and chronic infections. We therefore used SEM to detect biofilm formation on implants harvested at 5 weeks after orthopedic surgery. As shown in Figure 6c, treatment with aNM@MPS reduced the overall propensity for biofilm formation, whereas implants taken from other groups of treated mice, especially the control and Van-treated groups, had dense biofilm aggregates. The bacterial colonies from rolling plate assays of the implant in the femur also revealed a significant reduction in the aNM@MPS group (Figure S17, Supporting Information), providing clear evidence that the biofilms on the implants were nearly eliminated by the biofunctional nanosheets. In addition, Gram staining for the evaluation of infection in bone tissue revealed no obvious MRSA infiltration in the aNM@MPS group (Figure 6d). Given that the production of host leukocyte IL-10 is an associated pathological feature of the persistence of *S. aureus* biofilm,[21a,26] we further detected the secretion of IL-10 in the peri-implant bone tissue via immunohistochemical staining with anti-IL-10. As shown in Figure 6e and Figure S18 (Supporting Information), the aNM@MPS treated group showed minimal IL-10 expression, with few positively stained areas at the infectious sites, while many IL-10-positive areas were detected in the other groups. Taken together, the biofunctional nanosheet treatment markedly alleviated hematogenous osteomyelitis in vivo.

S. aureus hematogenous osteomyelitis is a major factor impeding osteogenesis.[27] Suitable osteogenesis at the bone-implant interface is key to the postoperative evaluation of orthopedic surgery. The histology showed marked bone erosion in the control, Van-, and MPS-NSs-treated groups, while an almost complete bone structure was observed in the aNM@MPS-treated group (Figure S19, Supporting Information). The profile of the newly formed bone tissue around the implant was further studied via Masson's trichrome staining. We observed a significant presence of dense new bone at the bone–implant interfaces in the aNM@MPS group, in contrast to the sporadic formation of new bone seen in the other three groups (Figure 6f). The superior ability of aNM@MPS to sustain novel collagen synthesis can be attributed mainly to the long-lasting multiple protection mechanism, which successfully blocks the growth and colonization of surrounding bacteria, resulting in the preferential occupancy of biomaterial surfaces by host cells.

3. Discussion

Current clinical treatments for osteomyelitis are palliative, and they still rely largely on multiple antibiotics, long-term therapy, and extensive debridement surgery.[1a] Despite multidisciplinary approaches, more than one-third of osteomyelitis patients are not cured.[2a] In addition, currently available therapies often lead to systemic toxicity and even functional impairment.[28] Although osteomyelitis is a heterogeneous disease, critical clinical pathogenic insights indicate the persistence of multidrug-resistant bacteria during osteomyelitis formation and aggravation. Among these multidrug-resistant bacteria, *S. aureus*, especially MRSA strains, is the most causative pathogenic bacterium regarding osteomyelitis.[1a,29] *S. aureus* persistence reduced susceptibility to antibiotics and resulted in host immune defense paralysis via the formation of intracellular infection,[3] biofilm,[25,30] small-colony variants,[31] and osteocyte lacunocanalicular network invasion.[32] Macrophages, an essential component of the innate immune system, are critical to the innate immune response to *S. aureus*, initiating their bacterial killing activity after internalizing the pathogen, thus forming a bridge to the adaptive immune system.[8,33] Upon host immune defense paralysis, however, the macrophages-mediated immune defense mechanism is not commonly activated, favoring persistent infection.[7] Based on the above research findings, we developed biofunctional nanosheets to arm dysfunctional macrophages and allow them to terminate persistent infection-initiated pathological cascades, which could serially destroy invading organisms and elicit acquired bactericidal immune responses, thereby conferring an osteoprotective effect and ultimately eliminating osteomyelitis.

Osteomyelitis is a bone-infecting disease caused by infections due to orthopedic surgery or systemic bacteremia.[2a] Tracking and targeting dysfunctional macrophages at osteomyelitis sites is of utmost importance for the treatment of this skeletal system disease. Developing biohybrid micro/nanocarriers for active drug delivery provides a promising strategy.[34] Bone is a vascularized tissue rich in blood vessels,[35] which can be exploited for bone marrow-targeting drug delivery. Aged neutrophils have the inherent bone marrow homing under the guidance of the CXCR4/CXCL12 signal axis.[9a] At the end of this pathway, aNEs are safely removed by macrophage phagocytosis in the bone marrow, which mainly depends on macrophage-mediated programmed cell removal.[11a] Therefore, we proposed

Figure 5. aNM@MPS-enabled anti-infection and immunity activation effects in vivo. a) Therapeutic regimen in an implant-related osteomyelitis mouse model. b) Representative images of intracellular MRSA colony counting plates of the bone marrow aspirates after different treatments ($n = 3$ biologically independent animals per group). c) Quantitively intracellular MRSA burden in the bone marrow after the different treatments. Data are the mean ± s.d. ($n = 3$ biologically independent animals per group). d) Histological analysis with H&E staining of the bone tissues surrounding the implants ($n = 3$ biologically independent animals per group). Scale bar, 100 µm. e) Gram staining of the bone tissues surrounding the implants. Blue arrows indicate infiltrated bacteria ($n = 3$ biologically independent animals per group). Scale bar, 50 µm. f,g) Representative flow cytometry plots (f) and quantitative analysis (g) of $CD11b^+Gr\text{-}1^+$ MDSCs in MRSA-infected bone tissues at the study endpoint. Data are the mean ± s.d. ($n = 3$ biologically independent animals per group). h,i) Flow cytometry quantitative analysis of M1-like macrophages ($F4/80^+CD80^+$) (h) and M2-like macrophages ($F4/80^+CD206^+$) (i) in the peri-implant bone tissues of osteomyelitis mice in the indicated treatment groups. Data are the mean ± s.d. ($n = 3$ biologically independent animals per group). j,k) Flow cytometry quantitative analysis of the infiltration $CD3^+CD4^+$ (j) or $CD3^+CD8^+$ (k) T-cells in the peri-implant bone tissues of osteomyelitis mice in the indicated treatment groups. Data are the mean ± s.d. ($n = 3$ biologically independent animals per group). l) Peri-implant bone tissue sections were stained for OCN to determine the mature osteoblasts in osteomyelitis model mice treated with different formulations ($n = 3$ biologically independent animals per group). Scale bar, 50 µm. Nuclei were stained with DAPI (blue). m) Quantitative analysis of positive stained cells/areas of OCN. Data are the mean ± s.d. (n = 3 biologically independent animals per group). Statistical significance was determined by one-way ANOVA with Tukey's post hoc test for (c), (g), (h–k), and (m). $^*P < 0.05$, $^{**}P < 0.01$, $^{***}P < 0.001$, $^{****}P < 0.0001$.

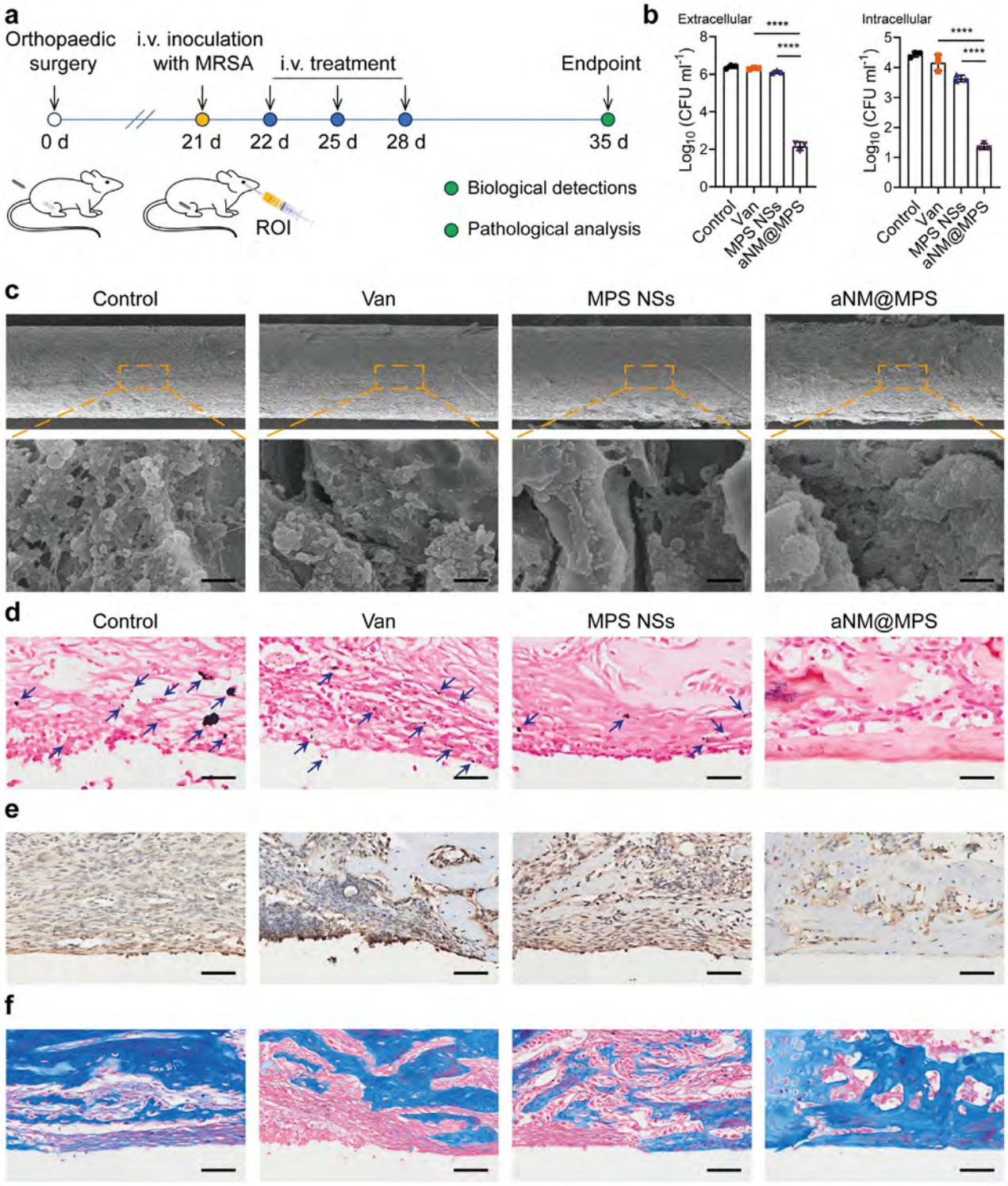

Figure 6. Effects of aNM@MPS on anti-hematogenous osteomyelitis. a) Therapeutic regimen in an MRSA-induced hematogenous implant-related osteomyelitis mouse model. ROI: retro-orbital injection. b) Bacterial burden in the bone marrow aspirates of the mice for the PBS, Van, MPS NSs, and aNM@MPS groups, respectively. Data are the mean ± s.d. ($n = 3$ biologically independent animals per group). c) SEM images were used to show the biofilms on the implant that was taken from infected bone tissue after treatment ($n = 3$ biologically independent animals per group). Scale bar, 4 μm. d) Gram staining of the bone tissues surrounding the implants. Blue arrows indicate infiltrated bacteria ($n = 3$ biologically independent animals per group). Scale bar, 50 μm. e) Immunohistochemical staining was used to detect the secretion of IL-10 in the infectious tissue of each group ($n = 3$ biologically independent animals per group). Scale bar, 100 μm. f) Sections of specimens stained with Masson's trichrome ($n = 3$ biologically independent animals per group). Scale bar, 100 μm. Statistical significance was determined by one-way ANOVA with Tukey's post hoc test for (b). ****$P < 0.0001$.

the aNM biomimetic strategy to meet the demand for bone marrow homing and serial in situ macrophage engineering. We demonstrated that aNM cloaking endowed nanosheets with enhanced bone marrow targeting ability (Figure 4a–e). Moreover, aNM-camouflaged nanosheets boosted internalization by macrophages both in vitro (Figure 3a–c) and in vivo (Figure 4f). The 2D $MnPSe_3$ nanosheets (MPS NSs) exhibited a manganese ions-mediated catalytic reaction that converted less toxic H_2O_2 into highly toxic •OH, effectively fueling oxidative capability (Figures 2h and 3f). Thus, the biofunctional nanosheet-armed macrophages showed the strongest bactericidal activity against intracellular bacteria (Figure 3g,h). The results are mainly attributed to the remarkable cellular internalization of the biofunctional nanosheets. This finding also explains one of the reasons for the failure of clinical therapies to eradicate intracellular infections: the poor cell membrane penetration of antibiotics.[4c] More importantly, manganese ions induced the activation of immune responses, especially the cGAS–STING signal pathway, resulting in the enhancement of macrophage-derived host-directed bactericidal immunity (Figures 3k–n and 5f–k; Figure S10, Supporting Information). In total, our data indicate that the biofunctional nanosheet-armed macrophages successfully enhanced the phagocytosis and digestion of MRSA intracellularly, preventing immune evasion and eliminating osteomyelitis synergistically.

As unique nanomaterials with a planar topology, 2D layered material-based nanoplatforms are an emerging class of biomaterials with remarkable potential for biomedical applications.[36] However, 2D layered materials must modulate their surface properties to break through biological barriers, such as blood–bone marrow barriers.[37] In general, non-spherical nanoformulations have shown prolonged blood circulation half-lives as compared to spherical ones.[38] The designed biofunctional nanosheets have a typical sheet-like core–shell structure (Figure 2c,e). The results demonstrate that biofunctional nanosheets with a cloaking property in the blood circulation can break through physiological barriers to achieve precise therapy. Importantly, the biofunctional 2D manganese-based nanosheets have satisfactory biosafety (Figures S6 and S12, Supporting Information). In subsequent work, we will systematically investigate the long-term fate of the biofunctional nanosheets in biological systems and their biological effects. Based on their superior biocompatibility and intriguing physicochemical properties, the biofunctional nanosheets, as a therapeutic platform, can successfully manage implant-associated or hematogenous osteomyelitis and thus prevent progressive bone destruction (Figures 5l,m and 6f). In addition, phosphorus- and selenium-containing materials are promising candidates for osteo-inductivity. The phosphorus element has been shown to facilitate biomineralization[39] and osteoblastic differentiation,[40] while the selenium element exhibits osteo-inductivity by accelerating angiogenesis and preventing osteolysis.[41] The significant expression of OCN, a key marker of osteogenic differentiation, in the aNM@MPS group indicates that the biofunctional 2D nanosheets enhance the availability of phosphorus and selenium at the osteomyelitis site, thereby promoting bone regeneration. Consequently, the biofunctional 2D $MnPSe_3$ nanosheets exhibit superior potential for managing refractory osteomyelitis in combination with bone defects.

The concept of aNM@MPS-based bone marrow–macrophage dual-targeting nanomedicine represents a frontier in osteomyelitis metalloimmunotherapy. Although the clinical translation of cell membrane-based biomimetic nanomedicines poses significant challenges, there are notable opportunities for aNM@MPS. To further advance future translational research, reliable derivation of aged neutrophil membranes and production of 2D nanomaterials can be envisioned through the application of standardized purification and preparation techniques commonly used in biologics. Following purification, the membrane coating process can be conducted using a microfluidic mixing technique to achieve finer control. After coating, the final aNM@MPS product can be lyophilized and stored for subsequent use. Previous studies have demonstrated that the cell membrane cloaking approach maintains viable storage stability.[42] Given the importance of preserving the structural integrity and functionality of biological membranes, developing specific cryoprotectants to maintain their stability is critical for long-term storage. Regarding cost-effectiveness, 2D nanomaterials can be readily sourced either from in-house production or commercial vendors. The high production costs of aged neutrophil membrane derivation can be mitigated by engineering universal cell lines. Additionally, the derivation of cell membranes and subsequent coating processes can leverage existing industrial-scale techniques to balance cost and quality. From an ethical standpoint, the derivation of cell membranes from patient autologous neutrophils mitigates many ethical concerns. In contrast, when cell membrane materials are obtained from allogeneic cells or genetically engineered cells, ethical considerations become significantly more complex and critical. Overall, with continued research, technological advances, and developments in precision medicine, we anticipate that the biofunctional nanosheets will be poised for widespread clinical adoption.

4. Conclusion

In summary, our findings show that macrophages in the skeletal infectious microenvironment can be targeted and reprogrammed for osteomyelitis treatment with the proposed manganese-based biofunctional 2D nanosheets. Using osteomyelitis mouse models, we demonstrated that dysfunctional macrophages in infected bone marrow can be precisely targeted in situ. Functionally, the aged neutrophil membrane biofunctional nanosheets effectively armed macrophages to kill intracellular bacteria and repolarized them to a proinflammatory phenotype in situ, serially eliciting host-directed bactericidal immune cascades and ultimately eradicating refractory osteomyelitis. Our work, therefore, provides a metalloimmunotherapy strategy for macrophage heterogeneity for osteomyelitis treatment, which may be extended to various macrophage-involving osteoimmune disorders, such as bone tumors, osteoporosis, and septic arthritis.

5. Experimental Section

Materials: Titanium implants (0.8 mm in diameter, 6 mm in length, 99.5% purity) were obtained from Baoji Henglongtai Metal Materials Co., Ltd. The 4′,6-diamidino-2-phenylindole (DAPI) kit, LysoTracker Green DND-26, 5(6)-Carboxyfluorescein diacetate succinimidyl ester, Percoll, Vancomycin and Gentamicin were provided by Beijing Solarbio Science & Technology Co., Ltd. 7-aminoactinomycin D, Rhodamine B isothiocyanate

(RBITC) and Recombinant murine macrophage colony-stimulating factor (M-CSF) was purchased from Beyotime Biotech Inc, Shanghai Haohong Scientific Co., Ltd and PeproTech Inc. Cell Staining Buffer, PE-labeled anti-CXCR4, FITC-labeled anti-Gr-1, PerCP-Cy5.5-labeled anti-CD11b, APC/Cy7-labeled anti-CD45, PE-labeled anti-CD4, APC-labeled anti-CD8, PE-labeled anti-CD11b, FITC-labeled anti-F4/80, PE-labeled anti-CD206, APC-labeled anti-CD80, and PE-labeled anti-CD86 antibodies were all purchased from BioLegend Inc. The anti-OCN and anti-IL10 antibodies for immunofluorescence or immunocytochemistry analysis were obtained from Servicebio or Cell Signaling Technology. All other chemicals and solvents of analytical grade were procured from local suppliers.

Cell Culture: Mouse neutrophils were collected from the bone marrow of C57BL/6 mice (7 weeks old, 22–24 g) using the Percoll gradient method.[10b] Briefly, bone marrow was rinsed with 1× phosphate-buffered saline (PBS), centrifuged at 450 g for 5 min, and the supernatant was discarded. The cells were precipitated with 4 mL 69% (vol/vol) Percoll and then superimposed on 4 mL 78% (vol/vol) Percoll, followed by centrifugation at 1600 g for 35 min. The cells from the interface of the 69% and 78% gradient layers were recovered to a new tube. Red blood cell lysis buffer was then added to the sample to lyse the erythrocytes. Neutrophils were purified by washing with ice-cold 1× PBS three times and resuspending the cells in a culture medium for aging. Cell purity was determined by flow cytometry after staining with APC/Cy7-labeled anti-CD45, PerCP-Cy5.5-labeled anti-CD11b, and FITC-labeled anti-Gr-1 antibodies.

Bone marrow-derived macrophages (BMDMs) were differentiated from mouse bone marrow monocytes in vitro.[43] The femurs and tibias were dissected from the C57BL/6 mice (7 weeks old, 22–24 g). Then, the bone marrow was rinsed with 1× PBS to isolate bone marrow cells, which was followed by erythrocyte lysis in red blood cell lysis buffer. After centrifugation, the cells were resuspended in a medium with M-CSF (20 ng mL^{-1}) to induce the maturation of BMDMs. After 3 d of incubation, the macrophage differentiation medium was discarded, and the plates were washed with 1× PBS to remove nonadherent cells. Adherent BMDMs were harvested at least 7 days after induction and used in subsequent experiments. The induction of mature macrophages was stained with PerCP-Cy5.5-conjugated anti-CD11b and FITC-conjugated anti-F4/80 antibodies and evaluated by flow cytometry (BD FACSAria III).

Aged Neutrophil Membrane Derivation: Neutrophils were further cultured in an incubator to obtain senescent neutrophils. After 0, 8, and 16 h, the cells were collected and stained with PE-labeled anti-CXCR4 and FITC-labeled anti-Gr-1 antibodies for 30 min. The unconjugated antibodies were washed off before the samples were detected by flow cytometry. Typically, aged neutrophil membranes are prepared from neutrophils that have been aged for 8 h in vitro. After washing with cold 1× PBS, the aged neutrophils were then resuspended in hypotonic lysing buffer containing protease inhibitor. Thereafter, the suspension was disrupted with a homogenizer for 5 min to obtain the suspension, and the cell membrane was collected through gradient centrifugation. Finally, the obtained membrane material was stored in 0.2 mM EDTA at −80 °C for subsequent use.

Preparation and Characterization of the aNM-Cloaked Nanosheets: $MnPSe_3$ bulk crystals were synthesized via the chemical vapor transport method. Iodine was used as the transport medium. Specifically, manganese (99.95%), phosphorus (99.9999%), and selenium (99.9999%) were placed in quartz glass ampoule (40×220 mm) in a stoichiometric ratio corresponding to 20 g of $MnPSe_3$ together with 0.5 g of iodine (99.9%) and 1 at.% excess of phosphorus and selenium. After melting and sealed under high vacuum ($<1\times10^{-3}$ Pa), the ampoule was first placed in a muffle furnace and heated at 450 °C for 25 h and subsequently at 500 °C for 50 h and on 600 °C for 50 h. Then the ampoule was transferred to a two-zone horizontal furnace. First, the growth zone was kept at 750 °C while the source zone was at 600 °C for 2 d. The thermal gradient was reversed by keeping the temperature of the source zone at 700 °C and that of the growth zone at 600 °C for the following 14 d. During the cooling process, the growth zone was heated at 400 °C, while the source zone was kept under 150 °C for 2 h to remove excess phosphorus, selenium, and transport medium. Finally, the ampoule was opened in argon argon-filled glovebox, and growth crystals were collected.

The mechanical exfoliation method was applied to achieve the $MnPSe_3$ nanosheets. First, bulk $MnPSe_3$ crystals were suspended in water at a concentration of 4 mg mL^{-1}. Then, the suspension was treated with probe sonication in an ice bath for 6 h with a power of 800 W, with a cycle of 3 s on and 2 s off. The obtained solution was centrifuged for 10 min at 5000 rpm to remove large bulks. The resulting supernatant solution was collected and further washed with ethanol and water. The final exfoliated $MnPSe_3$ nanosheets (MPS NSs) were obtained. aNM cloaking was then accomplished by dispersing and fusing aNM vesicles with MPS NSs by sonication using a CJ-010S bath sonicator under an ice bath at a frequency of 40 kHz and a power of 120 W for 5 min.

The morphology of these nanosheets was verified using transmission electron microscopy (HT7700 Exalens). In addition, the size distribution of the aNM-coated nanosheets was measured using dynamic light scattering (ZEN 90 Zetasizer, Malvern). The cloaking of aNM to the MPS NSs was captured by fluorescence microscopy with two individual fluorescence channels, CFSE-labeled aged neutrophil membranes and RhB-labeled MPS NSs, respectively. Protein characterization was carried out using Coomassie blue staining and flow cytometry assay. Briefly, 10 µL of aNM fragments, the aNM@MPS, and MPS NSs were loaded into the well of sodium dodecyl sulfate-polyacrylamide gels. Coomassie Blue combined with Bio-imaging Systems (Tanon Chemi Dog 5200T) was used to image total protein. For flow cytometry assay of the presence of CXCR4 on the surface of aNM@MPS, the aNM vesicles and the aNM@MPS were resuspended in 2% bovine serum albumin solution for 30 min. After blocking, these nanosheets were centrifuged and co-incubated with PE-labeled anti-CXCR4 for 30 min. Then after washing with 1× PBS, both the samples were detected by flow cytometry. To determine the •OH generation, aNM@MPS solution with a final concentration of 10 µg mL^{-1} and terephthalic acid solution with a final concentration of 10 mM were configured in the reaction system with pH 7.4 and pH 5.0 + 0.1 mM H_2O_2 solution, respectively. The fluorescence intensity was detected at Ex/Em = 315/425 nm after reaction for 30 min.

Bacterial Culture and in vitro Intracellular Infection Model: MRSA (ATCC43300) was obtained from the BioSci Biotech (Hangzhou, China). Individual colonies were separated from the TSA plate and then added to fresh TSB to grow overnight (37 °C, 200 rpm) for in vitro or in vivo studies. The model of intracellular infection in vitro is developed following the previously reported approach.[19b] Briefly, the BMDMs were infected with the logarithmic phase MRSA (multiplicity of infection, 20:1) in DMEM containing 10% FBS for 2 h. Cells were washed three times with 1× PBS, and gentamicin (100 µg mL^{-1}) was added for 2 h to lyse the remaining extracellular bacteria, and then the intracellular bacteria model was constructed successfully.

Transwell Model Study: To explore the migration ability of aNM@MPS from vascular to bone marrow under the effect of CXCR4-CXCL12 axis, a Transwell kit (0.4-µm pore size, 24-well plate, NEST) was used. A monolayer of HUVECs (2×10^5 per insert) was seeded on the insert. The HUVECs were cultured until confluence, and then they were treated with 0.4 µg μL^{-1} lipopolysaccharide for 2 h to mimic the leaky sinusoidal inflammatory vasculature. CXCL12 (20 ng mL^{-1}) was added in the bottom chamber. After washing the HUVECs to remove redundant lipopolysaccharides, RhB-labeled MPS NSs or aNM@MPS were seeded in the upper chamber for 4 h to study the translocation ability of the biofunctional nanosheets. The fluorescence intensity of nanosheets loading RhB in the bottom chamber was determined at Ex/Em = 555/580 nm.

Macrophage Targeting Abilities of the aNM@MPS In Vitro: BMDMs were seeded in confocal dishes and allowed to adhere overnight. The biofunctional nanosheets were then added to the cells. After incubation for 2 h, the cells were washed 3 times with ice-cold 1× PBS and fixed with 4% paraformaldehyde. Then the cells were incubated at 37 °C for 15 min with 10 nM DAPI and imaged with LSM 980 with an Airyscan 2 Super-Resolution microscope (ZEISS, Germany). For flow cytometric analysis, the treated BMDMs were scraped and collected after PBS washing and then analyzed with a BD Biosciences flow cytometer. The results were analyzed using FlowJo software.

Evaluation on aNM@MPS Colocalization with Bacteria and •OH Generation in Macrophages: Colocalization of MRSA and aNM@MPS within macrophages were investigated by fluorescence microscope. First, macrophages that were pretreated with CFSE-prestained MRSA constructed an intracellular bacteria model as aforementioned. Then, the infected macrophages were treated with the RhB-labeled biofunctional nanosheets and co-cultured for 2 h. After that, the nucleus of infected macrophages was stained with 10 nM DAPI for 15 min. Then, the fluorescence images were captured by CLSM.

The fluorescent probe of •OH, hydroxyphenyl fluorescein, was employed to evaluate the aNM@MPS mediated cellular •OH generation after the nanosheets internalized by MRSA-infected BMDMs. The •OH signal was indicated by cell fluorescence intensity that was determined by flow cytometry and fluorescence microscope.

In vitro Antimicrobial Assay: Intracellular bacterial clearance by the biofunctional nanosheets was evaluated by the in vitro intracellular infection model. Infected macrophages were incubated with PBS, Van, MPS NSs, and aNM@MPS respectively. Cells incubated after 12 h, the cells in different treatments were then washed with PBS and lysed with 0.1% Triton X-100. The resulting lysates were cultured on TSA plates to quantify the bacterial colony-forming units (CFUs).

To evaluate whether the biofunctional nanosheets could enhance the phagocytosis efficiency of macrophages toward bacteria. MRSA was first stained with RhB in the dark for 30 min. Subsequently, BMDMs pretreated with PBS, Van, MPS NSs, and aNM@MPS were co-cultured with RhB-tagged MRSA at a 1:20 ratio. After 1.5 h of co-culture, the cells were harvested, stained with a FITC-conjugated anti-F4/80 antibody, and then analyzed by flow cytometry. For visualization purposes, CFSE-labeled PBS, Van, MPS nanoparticles, or aNM@MPS-armed macrophages were co-cultured with RhB-tagged MRSA at a 1:20 ratio for 2 h at 37 °C. The phagocytic levels were observed by fluorescence microscope.

Immunomodulation Effects of the aNM@MPS In Vitro: M2-BMDMs were seeded in 6-well plates and allowed to incubate for 24 h before PBS, Van, MPS NSs and aNM@MPS were added, respectively. Subsequently, the macrophages were exposed to different treatments overnight, followed by incubation in a fresh medium for 24 h. The cells were then harvested and rinsed with PBS three times, pre-blocked with CD16/32 antibodies (BioLegend, dilution ratio 1:100) for 10 min at room temperature for Fc receptors blockade, and stained with the different antibodies according to the instructions of the manufacturer's instructions. The $F4/80^+CD206^+$ (M2) or $F4/80^+CD80^+$ (M1) or $CD80^+CD86^+$ populations were determined using flow cytometry (BD FACSAria III), and the results were analyzed using FlowJo software.

The immunomodulation efficiency of the biofunctional nanosheets was also investigated by quantitative real-time PCR (qRT-PCR). After different treatments, the total mRNA was extracted by TRIzol reagent (Invitrogen), and reversely transcribed into cDNA by a SuperRTIII All-in-one RT Mix (biosharp). RT-qPCR was performed with Universal SYBR qPCR Master Mix (biosharp) by QuantStudio 5 (Applied Biosystems). The related gene expressions of TNF-α, IL-10, IFN-β, cGAS, STING, and CXCL10 were tested and β-actin was used as a housekeeping gene. The assay was quantitatively calculated by the $2^{-\Delta\Delta Ct}$ method. qRT-PCR was performed using specific primers (Table S1, Supporting Information).

Study on the Biodistribution of the aNM@MPS in Osteomyelitis Mouse Model: All animal studies were performed following the protocols approved by the Beijing Institute of Technology Institutional's Animal Care and Use Committee and in compliance with all relevant ethical regulations (License No: BIT-EC-SCXK (Beijing), 2019-0010-M-054). The biodistribution of the biofunctional nanosheets in mice was quantified using an IVIS system (CRI, Inc., excitation: 748 nm, optical filter: 780 nm). The DiR-labeled MPS NSs and aNM@MPS were intravenously injected into osteomyelitis mice via the tail vein. At predetermined times, the mice were sacrificed to obtain hind limb long bone, heart, liver, spleen, lungs, and kidneys for analysis.

To observe the specific bone marrow homing of the biofunctional nanosheets, RhB-labeled aNM@MPS with a dose of 2.5 mg kg^{-1} was injected into osteomyelitis mice, with free RhB-labeled MPS NSs as a control. After 48 h, the mice were euthanized, and the femur was obtained and fixed with 4% paraformaldehyde at 4 °C for 48 h. Then, the paraffin-embedded bone tissue sections were prepared and the slides were stained with anti-F4/80 antibodies, followed by DAPI staining. Fluorescence imaging was performed by CLSM.

Biosafety Analysis: For in vitro cytotoxicity experiments, a cell counting kit-8 (CCK8) assay was used to evaluate the cytocompatibility following various dose treatments of aNM@MPS. To investigate the biocompatibility of the biofunctional nanosheets in vivo, the animals from the titanium-based bone implanted mouse model were treated with PBS or aNM@MPS (10 mg kg^{-1}) three times in one week and euthanized at the study endpoint. Fresh whole blood from these mice was collected on day 28 for routine blood tests and the detection of biochemical markers. The femur bone tissues surrounding the implants, heart, liver, spleen, lungs, and kidneys were excised and fixed in 10% formalin for 48 h for histological analyses.

Bactericidal Effects of the aNM@MPS in Implant-Related Osteomyelitis Model: An implant-related osteomyelitis mouse model was established by the following protocol.[23] Mice were anesthetized using inhalational isoflurane (1–5%) mixed with oxygen. The distal femur was exposed via a medial parapatellar arthrotomy, with lateral displacement of the quadriceps-patellar complex. Then, a burr hole was created in the femoral mid-shaft with a 25-gauge needle. Following a total of 2 µL of MRSA suspension (1×10^5 CFUs mL^{-1}) inoculated in the bone marrow cavity, the medical-grade titanium implant (0.8 mm diameter and 6 mm length) was inserted to model orthopedic implant-related osteomyelitis.

To evaluate the therapeutic effects in the intracranial implant-related osteomyelitis mouse model, four different treatments PBS (100 µL), vancomycin (20 mg kg^{-1}), MPS NSs (10 mg kg^{-1}), and aNM@MPS (10 mg kg^{-1} MPS NSs equivalent dose) were administered via the tail vein three times a week from day 1 to 7. On day 14 after bacteria inoculation, three mice from each group were euthanatized, and the implanted femora were harvested for bacterial colony counting. Particularly, bacteria isolated from the implants and bone marrow aspirate suspensions served as extracellular bacteria. Bacteria were isolated from the aseptically homogenized bone marrow cell population as intracellular bacteria. Meanwhile, another three implanted femora tissues were harvested and sectioned for H&E and Gram staining.

Flow Cytometry Assay In Vivo: On day 7 after the last injection with the indicated formulations, the treated mice from each group were sacrificed to analyze the profiles of immune cells in the bone marrow around infection lesions. The peri-implant bone marrow was dispersed and filtered to obtain single-cell suspensions. The cell suspension was washed with 1× PBS and lysed the erythrocytes. Then, the cell suspension was incubated with CD16/32 (BioLegend, dilution ratio 1:100) for 10 min to block nonspecific antibody binding, followed by staining with various antibodies as per the manufacturer's instructions. The $CD11b^+Gr\text{-}1^+$ (MDSCs) or $F4/80^+CD206^+$ (M2) or $F4/80^+CD80^+$ (M1) or $CD3^+CD4^+$ T cells or $CD3^+CD8^+$ T cells populations were determined using flow cytometry (BD FACSAria III), and the results were analyzed using FlowJo software.

Mouse Hematogenous Osteomyelitis Model Study: The mouse hematogenous osteomyelitis model was established on the titanium-based bone implanted mouse model.[44] The mouse femoral implant model was first established as described above. At 21 d post-surgery, 100 µL MRSA at 2×10^5 CFUs mL^{-1} was inoculated via retro-orbital injection (ROI). On day 22, the mice in each group were injected into the tail vein with PBS (100 µL), vancomycin (20 mg kg^{-1}), MPS NSs (10 mg kg^{-1}), and aNM@MPS (10 mg kg^{-1} MPS NSs equivalent dose) three times within 7 days. Seven days after the third administration, the treated hematogenous osteomyelitis mice were euthanized for further analysis, including the antibacterial activities evaluation and biofilm detection.

Histopathological, Immunofluorescence, and Immunohistochemical Analyses: At the study endpoint, implanted femora tissues were harvested and then fixed with 4% paraformaldehyde. After decalcified by EDTA decalcifying solution, these bone tissues dehydrated in an ascending graded series of ethanol solutions, and embedded in paraffin. H&E, Gram, and Masson's trichrome staining were carried out following the manufacturer's instructions provided with the kits. For immunofluorescence analysis, the

sectioned tissues were stained overnight with primary antibodies against OCN (Servicebio) at 4 °C. The samples were then incubated with an appropriate secondary antibody labeled with Cy3 for 2 h, followed by counterstaining with DAPI. To detect IL-10 expression, implanted femora tissue sections were dewaxed and stained with anti-IL-10 primary antibodies (Servicebio). Biotinylated goat anti-rabbit IgG was used as the secondary antibody for chromogen development. The relative quantification of osteoblasts and the area of IL-10 positively stained regions were evaluated with Image J software (http://imagej.net/).

Statistical Analysis: The results are presented as mean ± s.d. Error bars represent the s.d. of the mean from independent samples. Two-tailed Student's *t* test was applied to test the statistical significance of differences between the two groups. Statistically significant differences among the groups were analyzed using one-way analysis of variance (ANOVA). GraphPad Prism 9.0 (GraphPad Software Inc.) and Microsoft Excel 2021 (Microsoft Inc.) were used for all statistical analysis. Statistical significance was set at $^{*}P < 0.05$, $^{**}P < 0.01$, $^{***}P < 0.001$, $^{****}P < 0.0001$.

Supporting Information

Supporting Information is available from the Wiley Online Library or from the author.

Acknowledgements

J.L. acknowledged the financial support from the Beijing Nova Program of Science and Technology (20240484527), the National Natural Science Foundation of China (52302343), and the Beijing Institute of Technology Teli Young Fellow Program (RCPT-20220029). Z.S. was supported by the ERC-CZ program (project LL2101) from the Ministry of Education Youth and Sports (MEYS) and by the project Advanced Functional Nanorobots (reg. No. CZ.02.1.01/0.0/0.0/15_003/0000444 financed by the EFRR). P.K.C. acknowledged the financial support from the City University of Hong Kong Donation Research Grants (9220061 and DON-RMG 9229021). The authors thank the Biological and Medical Engineering Core Facilities of the Beijing Institute of Technology for supporting experimental equipment.

Conflict of Interest

The authors declare no conflict of interest.

Data Availability Statement

The data that support the findings of this study are available from the corresponding author upon reasonable request.

Keywords

biofunctional nanosheets, macrophage engineering, metalloimmunotherapy, osteomyelitis, phagolysosomal killing

Received: January 10, 2025
Revised: May 13, 2025
Published online: June 2, 2025

[1] a) E. A. Masters, B. F. Ricciardi, K. L. d. M. Bentley, T. F. Moriarty, E. M. Schwarz, G. Muthukrishnan, *Nat. Rev. Microbiol.* **2022**, *20*, 385; b) M. Dudareva, A. J. Hotchen, J. Ferguson, S. Hodgson, M. Scarborough, B. L. Atkins, M. A. McNally, *J. Infection* **2019**, *79*, 189.

[2] a) N. Kavanagh, J. Ryan Emily, A. Widaa, G. Sexton, J. Fennell, S. O'Rourke, C. Cahill Kevin, J. Kearney Cathal, J. O'Brien Fergal, W. K Steven, *Clin. Microbiol. Rev.* **2018**, *31*, 00084; b) D. P. Lew, F. A. Waldvogel, *Lancet* **2004**, *364*, 369.

[3] A. R. Zelmer, R. Nelson, K. Richter, G. J. Atkins, *Bone Res.* **2022**, *10*, 53.

[4] a) T. J. Foster, *Nat. Rev. Microbiol.* **2005**, *3*, 948; b) T. W Fok Lung, I. R. Monk, K. P. Acker, A. Mu, N. Wang, S. A. Riquelme, S. Pires, L. P. Noguera, F. Dach, S. J. Gabryszewski, B. P. Howden, A. Prince, *Nat. Microbiol.* **2020**, *5*, 141; c) E. M. Darby, E. Trampari, P. Siasat, M. S. Gaya, I. Alav, M. A. Webber, J. M. A. Blair, *Nat. Rev. Microbiol.* **2023**, *21*, 280.

[5] a) M. J. Sweet, D. Ramnath, A. Singhal, R. Kapetanovic, *Nat. Rev. Immunol.* **2025**, *25* , 92; b) R. S. Flannagan, G. Cosío, S. Grinstein, *Nat. Rev. Microbiol.* **2009**, *7*, 355.

[6] a) T. R. McCulloch, T. J. Wells, F. Souza-Fonseca-Guimaraes, *Trends Microbiol.* **2022**, *30*, 158; b) J. Li, X. Jiang, H. Li, M. Gelinsky, Z. Gu, *Adv. Mater.* **2021**, *33*, 2004172.

[7] a) K. Krause, K. Daily, S. Estfanous, K. Hamilton, A. Badr, A. Abu Khweek, R. Hegazi, M. N. K. Anne, B. Klamer, X. Zhang, M. A. Gavrilin, V. Pancholi, A. O. Amer, *EMBO Rep.* **2019**, *20*, 48109; b) L. Chen, Z. Shao, Z. Zhang, W. Teng, H. Mou, X. Jin, S. Wei, Z. Wang, Y. Eloy, W. Zhang, H. Zhou, M. Yao, S. Zhao, X. Chai, F. Wang, K. Xu, J. Xu, Z. Ye, *Adv. Mater.* **2024**, *36*, 2304774.

[8] P. Orning, D. Weng, K. Starheim, D. Ratner, Z. Best, B. Lee, A. Brooks, S. Xia, H. Wu, M. A. Kelliher, S. B. Berger, P. J. Gough, J. Bertin, M. M. Proulx, J. D. Goguen, N. Kayagaki, K. A. Fitzgerald, E. Lien, *Science* **2018**, *362*, 1064.

[9] a) H. Garner, K. E. de Visser, *Science* **2017**, *358*, 42; b) M. Casanova-Acebes, C. Pitaval, L. A. Weiss, C. Nombela-Arrieta, R. Chèvre, N. A-González, Y. Kunisaki, D. Zhang, N. van Rooijen, L. E. Silberstein, C. Weber, T. Nagasawa, P. S. Frenette, A. Castrillo, A. Hidalgo, *Cell* **2013**, *153*, 1025.

[10] a) N. Borregaard, *Immunity* **2010**, *33*, 657; b) Z. Luo, Y. Lu, Y. Shi, M. Jiang, X. Shan, X. Li, J. Zhang, B. Qin, X. Liu, X. Guo, J. Huang, Y. Liu, S. Wang, Q. Li, L. Luo, J. You, *Nat. Nanotechnol.* **2023**, *18*, 647.

[11] a) M. Feng, K. D. Marjon, F. Zhu, R. Weissman-Tsukamoto, A. Levett, K. Sullivan, K. S. Kao, M. Markovic, P. A. Bump, H. M. Jackson, T. S. Choi, J. Chen, A. M. Banuelos, J. Liu, P. Gip, L. Cheng, D. Wang, I. L. Weissman, *Nat. Commun.* **2018**, *9*, 3194; b) J. S. Savill, A. H. Wyllie, J. E. Henson, M. J. Walport, P. M. Henson, C. Haslett, *J. Clin. Invest.* **1989**, *83*, 865.

[12] a) L. Li, L. Cao, X. Xiang, X. Wu, L. Ma, F. Chen, S. Cao, C. Cheng, D. Deng, L. Qiu, *Adv. Funct. Mater.* **2022**, *32*, 2107530; b) X. Guan, S. Wu, S. Ouyang, S. Ren, N. Cui, X. Wu, D. Xiang, W. Chen, B. Yu, P. Zhao, B. Wang, *Adv. Healthcare Mater.* **2024**, *13*, 2303529; c) L. Li, Y. Yin, S. Zhang, J. Yang, P. Li, H. Zhou, J. Li, *BMEMat* **2024**, *2*, 12081.

[13] a) X. Sun, X. Zhou, X. Shi, O. A. Abed, X. An, Y. L. Lei, J. J. Moon, *Nat. Biomed. Eng.* **2024**, *8*, 1073; b) H. Lei, Q. Li, G. Li, T. Wang, X. Lv, Z. Pei, X. Gao, N. Yang, F. Gong, Y. Yang, G. Hou, M. Chen, J. Ji, Z. Liu, L. Cheng, *Bioactive Mater.* **2024**, *31*, 53.

[14] a) C. Yang, Y. Luo, H. Shen, M. Ge, J. Tang, Q. Wang, H. Lin, J. Shi, X. Zhang, *Nat. Commun.* **2022**, *13*, 4866; b) A. Murali, G. Lokhande, K. A. Deo, A. Brokesh, A. K. Gaharwar, *Mater. Today* **2021**, *50*, 276; c) S. Zhang, H. Zhou, Y. Zhou, J. Li, J. Zhou, *Fundamental Research* **2024, DOI: 10.1016/j.fmre.2024.02.005**.

[15] a) E. Blanco, H. Shen, M. Ferrari, *Nat. Biotechnol.* **2015**, *33*, 941; b) L. Miao, Y. Wei, X. Lu, M. Jiang, Y. Liu, P. Li, Y. Ren, H. Zhang, W. Chen, B. Han, W. Lu, *Adv. Drug Delivery Rev.* **2024**, *204*, 115131.

[16] S. M. Lawrence, R. Corriden, V. Nizet, *Trends Immunol.* **2020**, *41*, 531.

[17] R. Kumar, R. N. Jenjeti, V. S. K. Choutipalli, V. Subramanian, S. Sampath, *Sens. Actuators, B* **2021**, *347*, 130633.

[18] Y. Liu, J. Wang, *Chem. Eng. J.* **2023**, *466*, 143147.

[19] a) C. Garzoni, W. L. Kelley, *Trends Microbiol.* **2009**, *17*, 59; b) X. Hou, X. Zhang, W. Zhao, C. Zeng, B. Deng, D. W. McComb, S. Du, C. Zhang, W. Li, Y. Dong, *Nat. Nanotechnol.* **2020**, *15*, 41.
[20] F. Gao, T. Shao, Y. Yu, Y. Xiong, L. Yang, *Nat. Commun.* **2021**, *12*, 745.
[21] a) C. E. Heim, M. E. Bosch, K. J. Yamada, A. L. Aldrich, S. S. Chaudhari, D. Klinkebiel, C. M. Gries, A. A. Alqarzaee, Y. Li, V. C. Thomas, E. Seto, A. R. Karpf, T. Kielian, *Nat. Microbiol.* **2020**, *5*, 1271; b) X. Zhang, T. Xiong, L. Gao, Y. Wang, L. Liu, T. Tian, Y. Shi, J. Zhang, Z. Zhao, D. Lu, P. Luo, W. Zhang, P. Cheng, H. Jing, Q. Gou, H. Zeng, D. Yan, Q. Zou, *Nat. Commun.* **2022**, *13*, 5493.
[22] S. Chen, A. F. U. H. Saeed, Q. Liu, Q. Jiang, H. Xu, G. G. Xiao, L. Rao, Y. Duo, *Signal Transduction Targeted Ther.* **2023**, *8*, 207.
[23] K. Li, Y. Chen, Y. Lin, G. Zhang, J. Su, X. Wu, C. Cheng, Y. Wang, B. Yu, X. Zhang, *Mol. Ther.* **2023**, *31*, 174.
[24] P. Sendi, F. Banderet, P. Graber, W. Zimmerli, *J. Infection* **2011**, *63*, 17.
[25] E. A. Masters, R. P. Trombetta, K. L. de Mesy Bentley, B. F. Boyce, A. L. Gill, S. R. Gill, K. Nishitani, M. Ishikawa, Y. Morita, H. Ito, S. N. Bello-Irizarry, M. Ninomiya, J. D. Brodell, C. C. Lee, S. P. Hao, I. Oh, C. Xie, H. A. Awad, J. L. Daiss, J. R. Owen, S. L. Kates, E. M. Schwarz, G. Muthukrishnan, *Bone Res.* **2019**, *7*, 20.
[26] Z. Van Roy, P. Arumugam, B. P. Bertrand, D. D. Shinde, V. C. Thomas, T. Kielian, *Nat. Commun.* **2024**, *15*, 8965.
[27] D. Jaramillo, J. P. Dormans, J. Delgado, T. Laor, J. W. St Geme, *Radiology* **2017**, *283*, 629.
[28] L. Ma, Y. Cheng, X. Feng, X. Zhang, J. Lei, H. Wang, Y. Xu, B. Tong, D. Zhu, D. Wu, X. Zhou, H. Liang, K. Zhao, K. Wang, L. Tan, Y. Zhao, C. Yang, *Adv. Mater.* **2024**, *36*, 2307846.
[29] a) B. Zhang, H. Zhang, Y. Sun, L. Chen, K. Sun, Y. Zhang, X. Hu, K. Zhao, Z. Wu, Y. Tang, *Adv. Healthcare Mater.* **2024**, *14* ,2403058; b) B. M. Bakadia, R. Zheng, A. A. Qaed Ahmed, Z. Shi, B. L. Babidi, T. Sun, Y. Li, G. Yang, *Adv. Healthcare Mater.* **2024**, *13*, 2304572.
[30] H. Zhou, Y. Ren, K. Zou, Y. Jin, H. Liu, H. Jiang, L. Shi, X. Sheng, J. Weeks, H. Wang, T. Xue, E. M. Schwarz, C. Xie, Z. Deng, L. Wang, L. Chu, *Adv. Healthcare Mater.* **2024**, *14*, 2403261.
[31] C. Kahl Barbara, K. Becker, B. Löffler, *Clin. Microbiol. Rev.* **2020**, *29*, 401.
[32] K. L. de Mesy Bentley, R. Trombetta, K. Nishitani, S. N. Bello-Irizarry, M. Ninomiya, L. Zhang, H. L. Chung, J. L. McGrath, J. L. Daiss, H. A. Awad, S. L. Kates, E. M. Schwarz, *J. Bone Miner. Res.* **2017**, *32*, 985.
[33] Z. Li, S. Zhang, Z. Fu, Y. Liu, Z. Man, C. Shi, C. Tang, C. Chen, Q. Chai, Z. Yang, J. Zhang, X. Zhao, H. Xu, M. Han, Y. Wang, Z. Liao, G. Yu, B. Shi, K. Zhao, W. Li, X. Jiang, *Sci. Adv.* **2023**, *9*, adg3365.
[34] a) R. H. Fang, A. V. Kroll, W. Gao, L. Zhang, *Adv. Mater.* **2018**, *30*, 1706759; b) S. Zhang, Q. Chai, Z. Man, C. Tang, Z. Li, J. Zhang, H. Xu, X. Xu, C. Chen, Y. Liu, F. Guo, M. Abdalla, G. Yu, K. Zhao, B. Shi, W. Li, X. Jiang, *Chem. Eng. J.* **2022**, *435*, 134848; c) J. Li, H. Zhou, C. Liu, S. Zhang, R. Du, Y. Deng, X. Zou, *Aggregate* **2023**, *4*, 359.
[35] a) S. Yin, W. Zhang, Z. Zhang, X. Jiang, *Adv. Healthcare Mater.* **2019**, *8*, 1801433; b) Y. Gai, Y. Yin, L. Guan, S. Zhang, J. Chen, J. Yang, H. Zhou, J. Li, *Cyborg and Bionic Systems* **2023**, *4*, 0058.
[36] J. Ouyang, S. Rao, R. Liu, L. Wang, W. Chen, W. Tao, N. Kong, *Adv. Drug Delivery Rev.* **2022**, *185*, 114268.
[37] a) C.-F. Mu, J. Shen, J. Liang, H.-S. Zheng, Y. Xiong, Y.-H. Wei, F. Li, *Biomaterials* **2018**, *155*, 191; b) T. Itkin, S. Gur-Cohen, J. A. Spencer, A. Schajnovitz, S. K. Ramasamy, A. P. Kusumbe, G. Ledergor, Y. Jung, I. Milo, M. G. Poulos, A. Kalinkovich, A. Ludin, K. Golan, E. Khatib, A. Kumari, O. Kollet, G. Shakhar, J. M. Butler, S. Rafii, R. H. Adams, D. T. Scadden, C. P. Lin, T. Lapidot, *Nature* **2016**, *532*, 323.
[38] J. Bariwal, H. Ma, G. A. Altenberg, H. Liang, *Chem. Soc. Rev.* **2022**, *51*, 1702.
[39] a) Y. Wang, X. Hu, L. Zhang, C. Zhu, J. Wang, Y. Li, Y. Wang, C. Wang, Y. Zhang, Q. Yuan, *Nat. Commun.* **2019**, *10*, 2829; b) Y. Shuai, H. Lu, R. Lv, J. Wang, Q. Wan, C. Mao, M. Yang, *Adv. Healthcare Mater.* **2021**, *10*, 2001695.
[40] H. Tada, E. Nemoto, B. L. Foster, M. J. Somerman, H. Shimauchi, *Bone* **2011**, *48*, 1409.
[41] a) X. Zhang, J. Huang, J. Huang, Z. Shi, H. Niu, Y. Zheng, X. Wang, C. Wu, J. Chen, P. Liu, Y. Zhu, *Adv. Funct. Mater.* **2025**, *35*, 2417871; b) B. Zou, Z. Xiong, Y. Yu, S. Shi, X. Li, T. Chen, *Adv. Mater.* **2024**, *36*, 2401620; c) Z. Xiong, H. Lin, H. Li, B. Zou, B. Xie, Y. Yu, L. He, T. Chen, *Adv. Funct. Mater.* **2023**, *33*, 2212970.
[42] a) C.-M. J. Hu, R. H. Fang, K.-C. Wang, B. T. Luk, S. Thamphiwatana, D. Dehaini, P. Nguyen, P. Angsantikul, C. H. Wen, A. V. Kroll, C. Carpenter, M. Ramesh, V. Qu, S. H. Patel, J. Zhu, W. Shi, F. M. Hofman, T. C. Chen, W. Gao, K. Zhang, S. Chien, L. Zhang, *Nature* **2015**, *526*, 118; b) C.-M. J. Hu, R. H. Fang, J. Copp, B. T. Luk, L. Zhang, *Nat. Nanotechnol.* **2013**, *8*, 336.
[43] S. Zhang, Y. Liu, W. Jing, Q. Chai, C. Tang, Z. Li, Z. Man, C. Chen, J. Zhang, P. Sun, R. Zhang, Z. Yang, M. Han, Y. Wang, X. Wei, J. Li, W. Li, M. Abdalla, G. Yu, B. Shi, Y. Zhang, K. Zhao, X. Jiang, *Nat. Commun.* **2023**, *14*, 817.
[44] Y. Wang, L. I. Cheng, D. R. Helfer, A. G. Ashbaugh, R. J. Miller, A. J. Tzomides, J. M. Thompson, R. V. Ortines, A. S. Tsai, H. Liu, C. A. Dillen, N. K. Archer, T. S. Cohen, C. Tkaczyk, C. K. Stover, B. R. Sellman, L. S. Miller, *Proc. Natl. Acad. Sci. USA* **2017**, *114*, E5094.

Supplementary Information

Manganese-based Biofunctional 2D Nanosheets Enabled in Situ Macrophage Engineering for Precise Eradication of Osteomyelitis

Shengchang Zhang, Huaijuan Zhou*, Bowen Chi, Zdenek Sofer, Paul K. Chu*, Yilong Wang, and Jinhua Li*

S. Zhang, J. Li
School of Medical Technology, Beijing Institute of Technology, Beijing 100081, China
E-mail: lijinhua@bit.edu.cn
H. Zhou
School of Interdisciplinary Science, Beijing Institute of Technology, Beijing, 100081, China
E-mail: huaijuan.zhou@bit.edu.cn
B. Chi, Y. Wang
Department of Neurology, Beijing Tiantan Hospital, Capital Medical University, Beijing 100070, China
Z. Sofer
Department of Inorganic Chemistry, University of Chemistry and Technology Prague, Prague 6 166 28, Czech Republic
P. K. Chu
Department of Physics, Department of Materials Science and Engineering, and Department of Biomedical Engineering, City University of Hong Kong, Tat Chee Avenue, Kowloon, Hong Kong 999077, China
E-mail: paul.chu@cityu.edu.hk

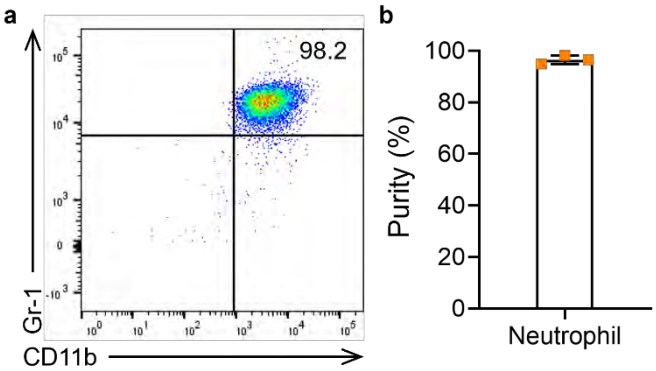

Figure S1. Flow cytometric analysis of the purity of neutrophils. **a.** Representative flow plots of $CD11b^{+}Gr\text{-}1^{+}$ neutrophils. **b.** The proportion of the $CD11b^{+}Gr\text{-}1^{+}$ neutrophils. Data are presented as the mean ± s.d. (n = 3 independent experiments).

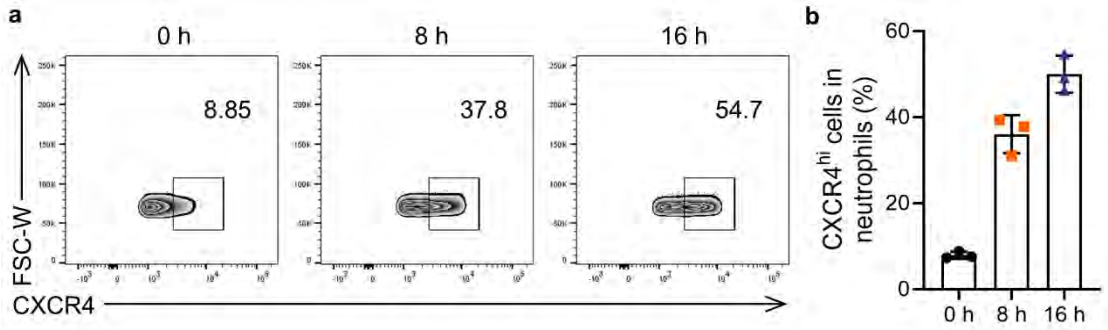

Figure S2. The CXCR4 expression on aged neutrophils over time. a. Representative flow plots of CXCR4^{+} neutrophils at 0 h, 8 h and 16 h. **b.** The proportion of CXCR4^{+} senescent neutrophils changed over time in vitro aging culture. Data are presented as the mean ± s.d. (n = 3 independent experiments).

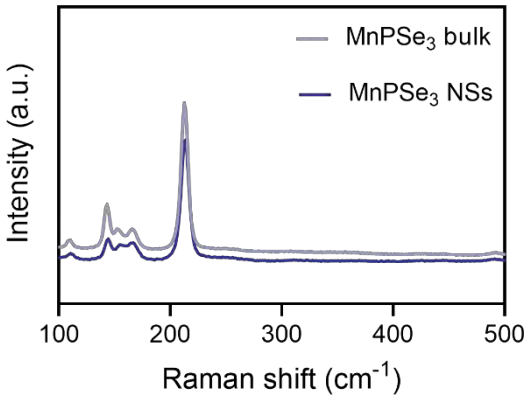

Figure S3. Raman spectra of bulk $MnPSe_3$ and the exfoliated MPS NSs.

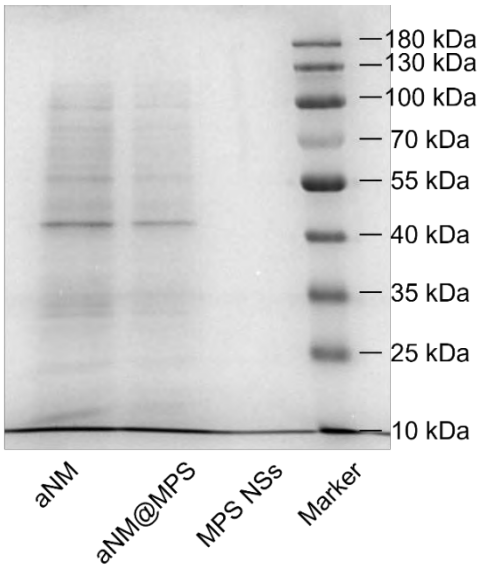

Figure S4. Protein profiles of membrane fragments, MPS NSs, and aNM@MPS characterized by SDS–polyacrylamide gel electrophoresis. (n = 3 independent experiments).

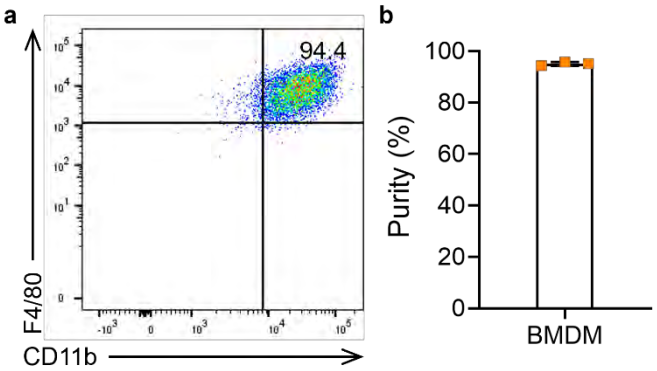

Figure S5. Flow cytometric analysis of the purity of BMDMs. a. Representative flow plots of $CD11b^{+}F4/80^{+}$ macrophages. **b.** The proportion of the $CD11b^{+}F4/80^{+}$ BMDMs. Data are presented as the mean ± s.d. (n = 3 independent experiments).

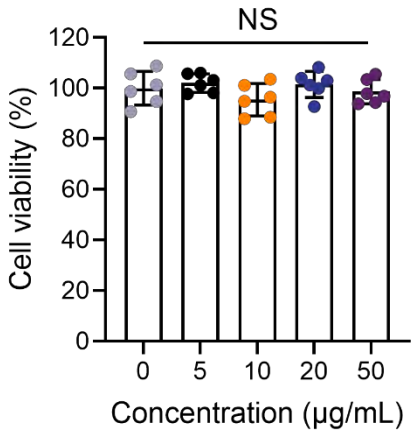

Figure S6. Biocompatibility of aNM@MPS was assessed with CCK-8 test. Data are presented as the mean ± s.d. (n = 6 independent experiments). Statistical significance was determined by one-way ANOVA with Tukey's post hoc test. NS, not significant.

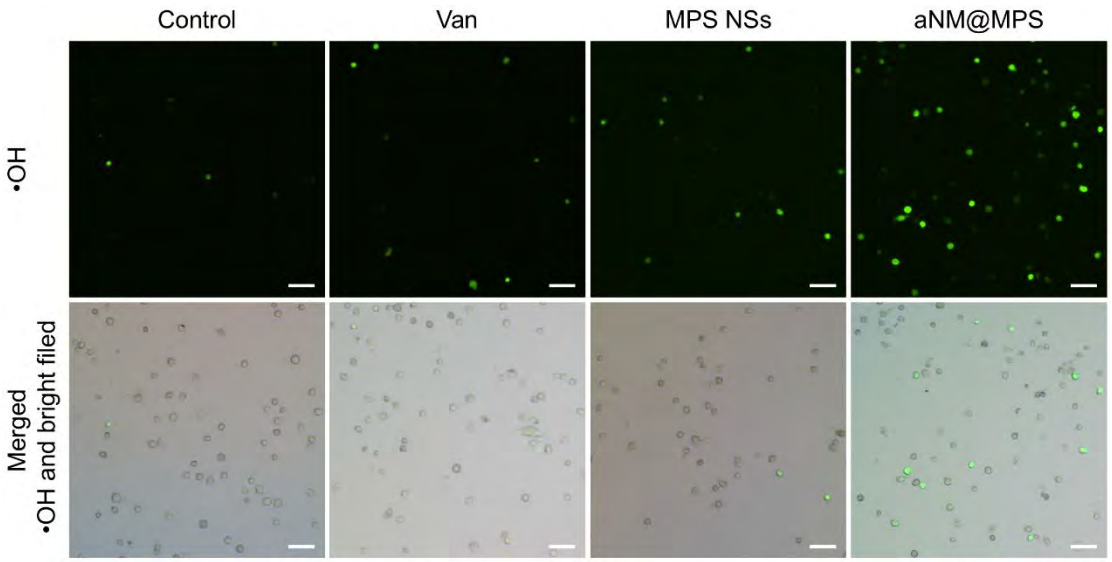

Figure S7. Fluorescent images of aNM@MPS induced •OH generation in macrophages. Scale bar, 100 μm. (n = 3 independent experiments).

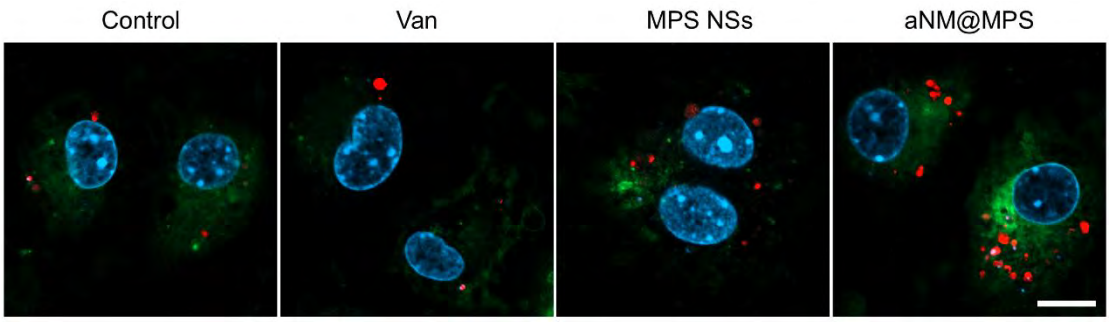

Figure S8. Representative images of the phagocytosis of MRSA by macrophages treated with each formulation. The red fluorescence shows phagocytosed MRSA, the green fluorescence shows macrophage, and the blue fluorescence shows nuclei. Scale bar, 10 μm.

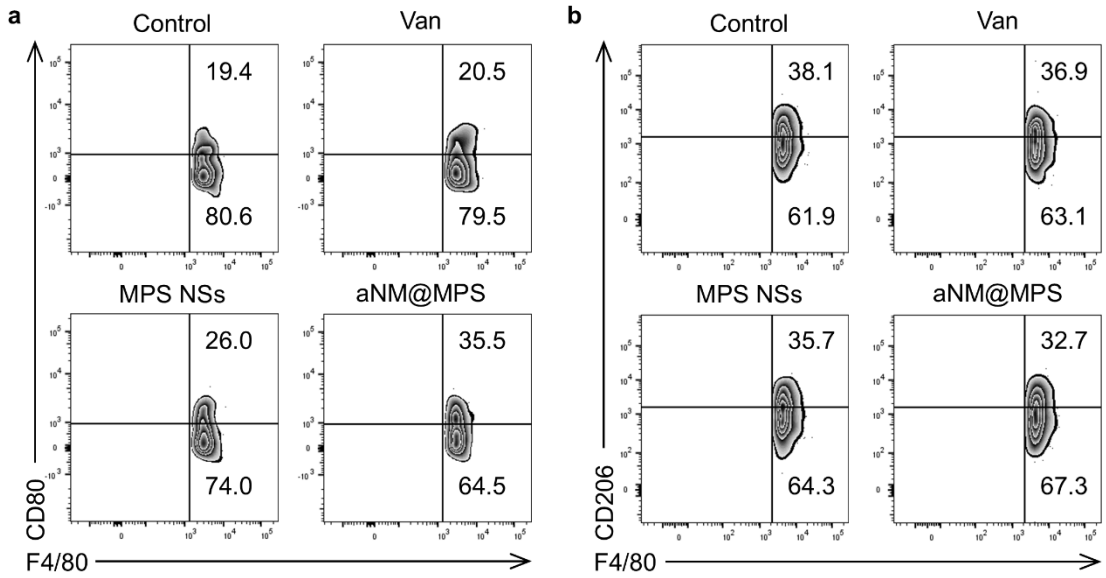

Figure S9. Flow cytometry analysis of macrophage phenotypes. Representative flow cytometry analysis of the percentages of $F4/80^{+}CD80^{+}$ (**a**) and $F4/80^{+}CD206^{+}$ (**b**) cells after treated with various formulations.

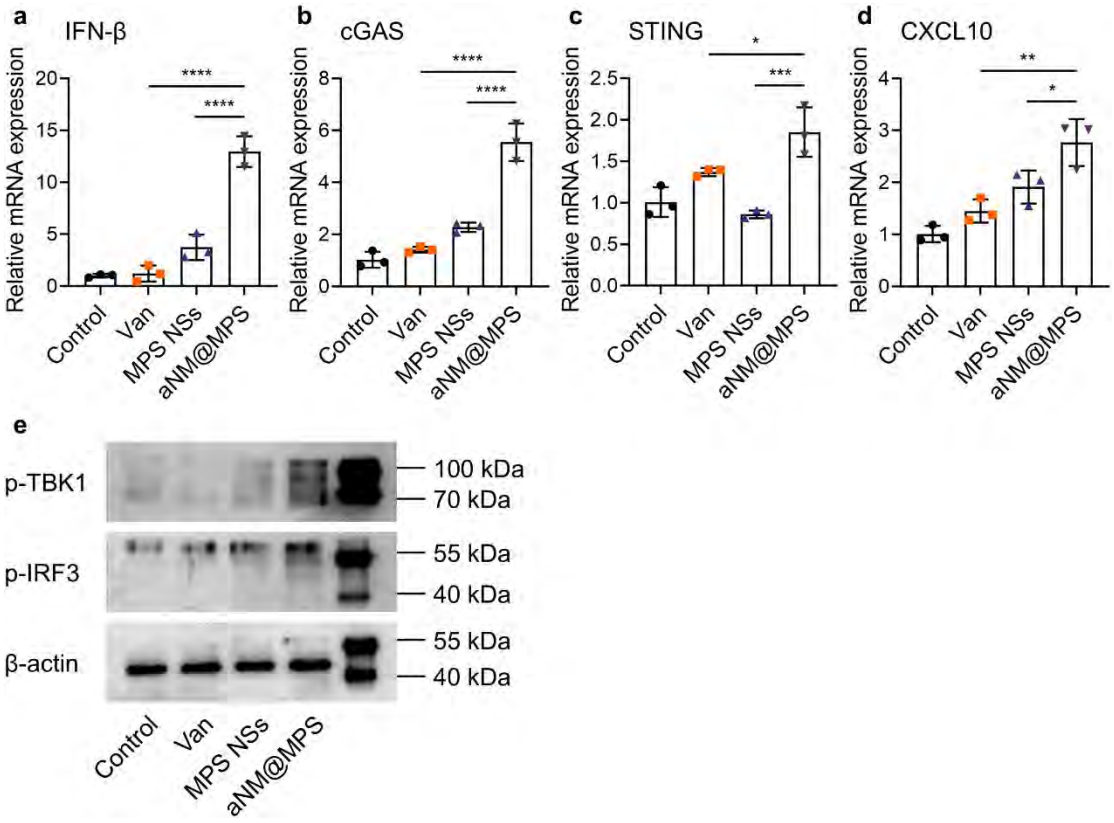

Figure S10. In vitro promotion of the cGAS-STING pathway. a. Statistical analysis of gene expression of IFN-β. The results are reported as the mean ± s.d. (n = 3 independent experiments). ****$P < 0.0001$. In vitro qRT-PCR analysis for the relative gene expression of cGAS-STING axis, including **b)** cGAS, **c)** STING, and **d)** CXCL10, in macrophages with different treatments. The results are reported as the mean ± s.d. (n = 3 independent experiments). Statistical significance was determined by one-way ANOVA with Tukey's post hoc test for **(a-d)**. *$P < 0.05$, **$P < 0.01$, ***$P < 0.001$, ****$P < 0.0001$. **e.** Western blot of the activation of the cGAS-STING pathway in macrophages after different treatments (n = 3 independent experiments).

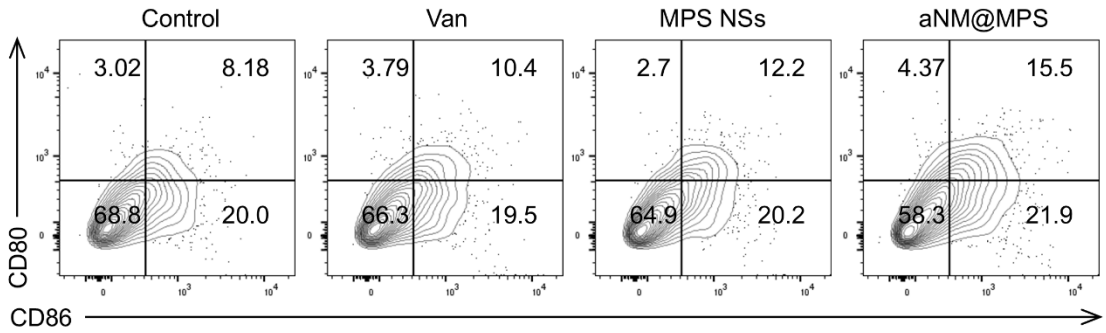

Figure S11. Representative flow cytometry plots of $CD80^{+}CD86^{+}$ cells from different treatment groups.

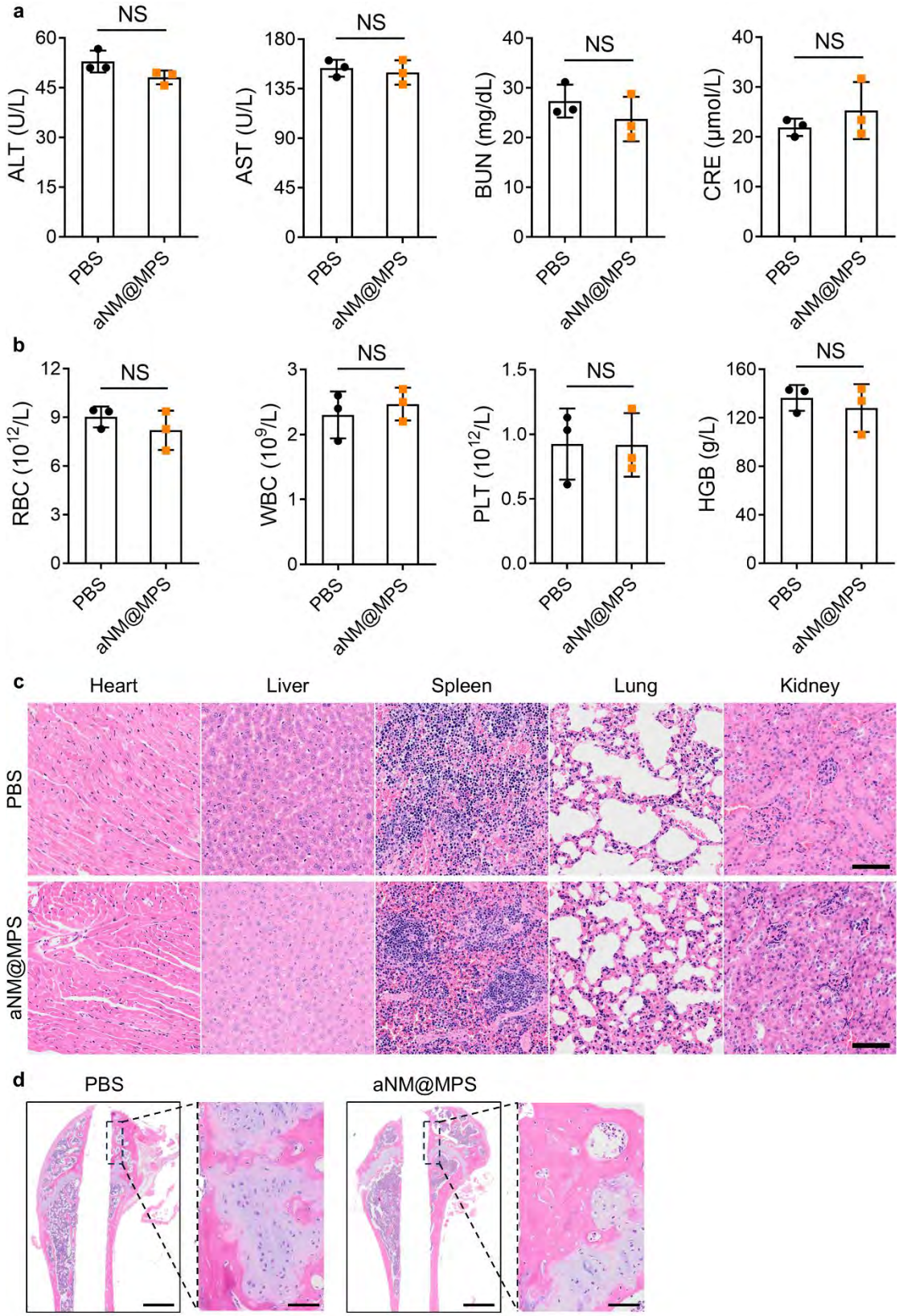

Figure S12. Systemic toxicity evaluation of aNM@MPS in vivo. Typical blood biochemical parameters (**a**) and routine blood parameters (**b**) of mice after receiving various treatments for 4 weeks. Data are presented as the mean ± s.d. (n = 3 biologically

independent animals). Statistical significance was determined by a two-sided Student's *t* test in **(a)** and **(b)**. NS, not significant. ALT, alanine aminotransferase; AST, aspartate aminotransferase; BUN, blood urea nitrogen; CRE, creatinine; RBC, red blood cell count; WBC, white blood cell; PLT, platelet; HGB, hemoglobin. **c.** Histological sections of major organs on the 28th day. Scale bar, 100 μm. (n = 3 biologically independent animals). **d.** Histological sections of the implanted femur on the 28th day. Scale bars, 500 and 50 μm. (n = 3 biologically independent animals).

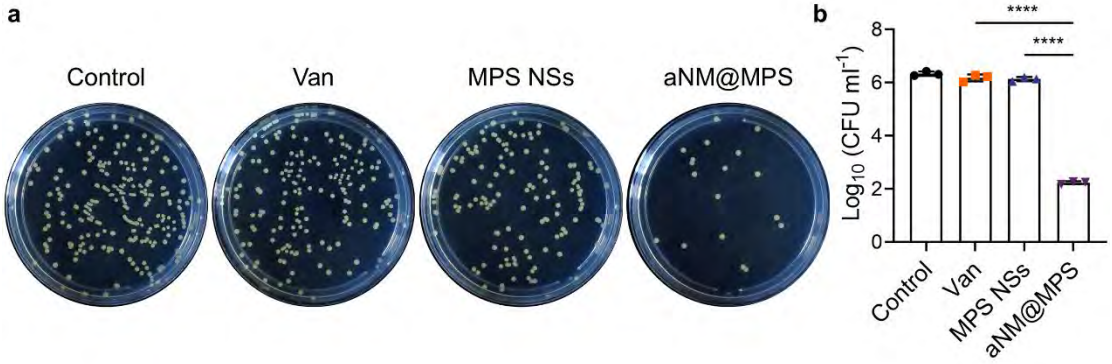

Figure S13. Quantitative results of extracellular MRSA in implant related osteomyelitis mice subjected to different treatments. a. Representative images of extracellular MRSA colony counting plates of the bone marrow aspirates after different treatments (n = 3 biologically independent animals per group). **b.** Quantitively extracellular MRSA burden in the bone marrow after the different treatments. Data are the mean ± s.d. (n = 3 biologically independent animals per group). Statistical significance was determined by one-way ANOVA with Tukey's post hoc test for **(b)**. ****$P < 0.0001$.

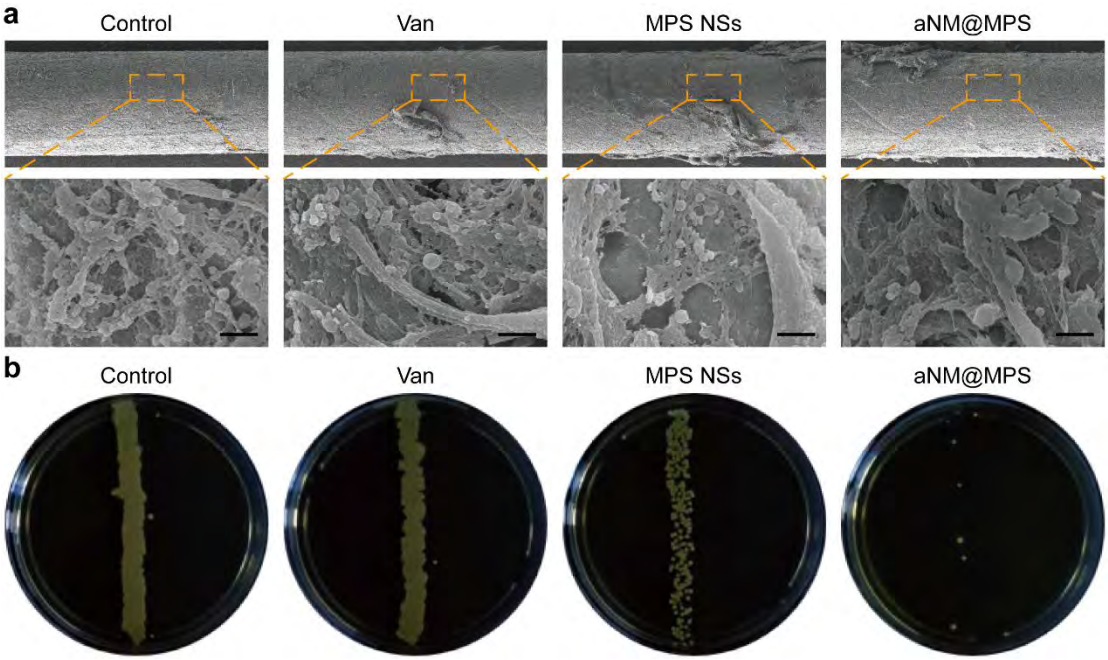

Figure S14 Representative general SEM images and optical images of bacterial colonies of the implant from the infected mice on day 14. a. Representative SEM images of the biofilm on the implant from the infected mice on day 14 (n = 3 biologically independent animals per group). Scale bar, 4 μm. **b.** Optical images of bacterial colonies after rolling the implant on agar plates (n = 3 biologically independent animals per group).

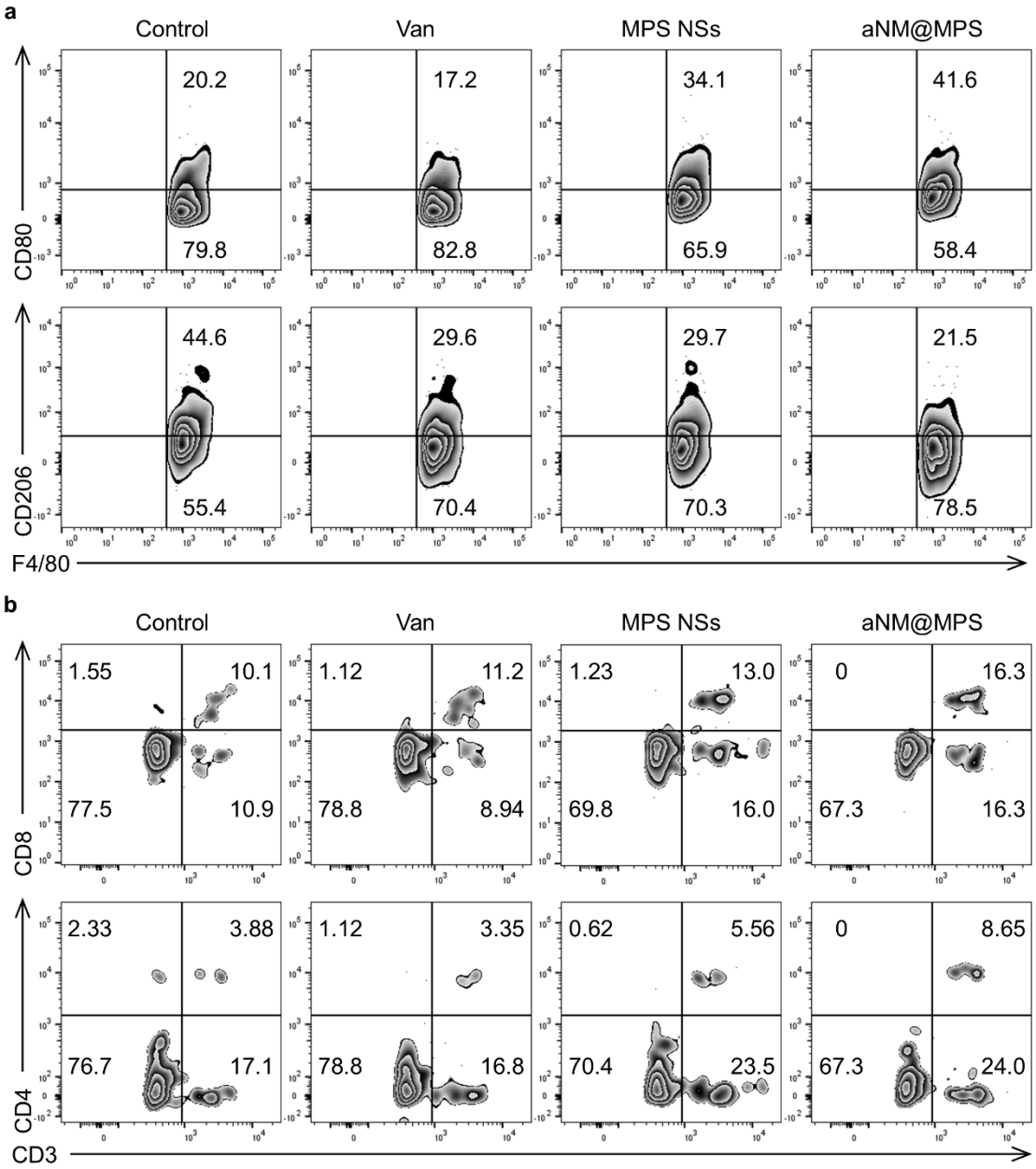

Figure S15. The immune cell landscape profile change in peri-implant bone after various treatments. a. Representative flow cytometry analysis of proinflammatory M1-like macrophages ($F4/80^+CD80^+$) and anti-inflammatory M2-like macrophages ($F4/80^+CD206^+$) in peri-implant bone of the mice treated with various formulations. **b.** Representative flow cytometry analysis of the percentages of $CD3^+CD8^+$ and $CD3^+CD4^+$ T cells in peri-implant bone of the mice treated with various formulations.

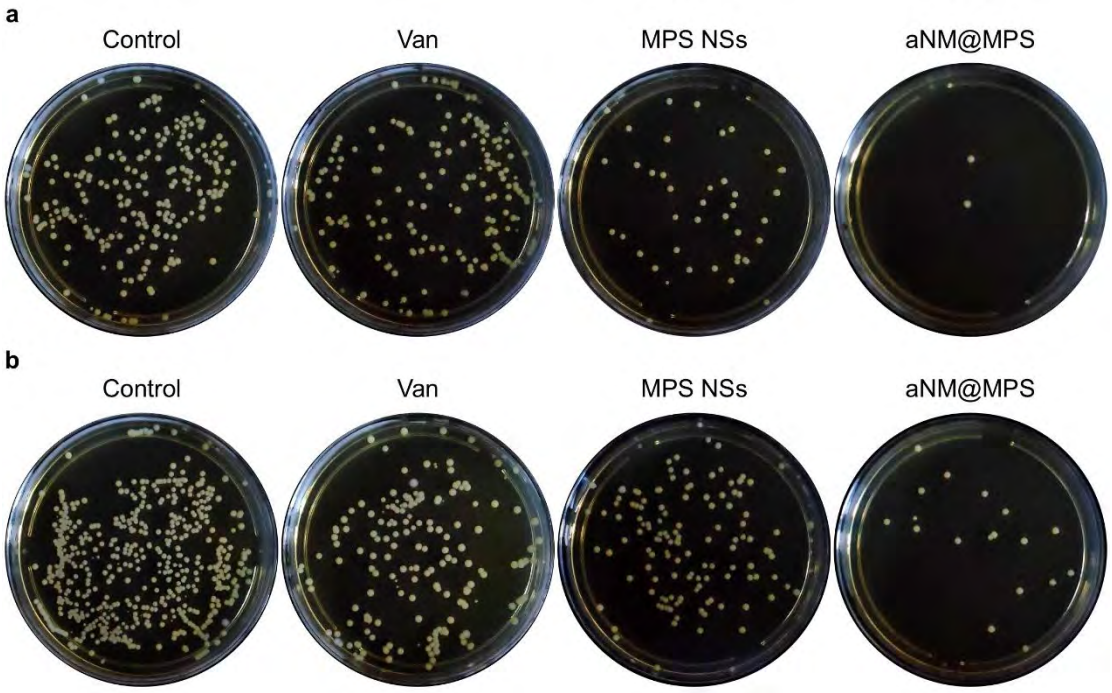

Figure S16. Representative photos of the bacterial colonies from the bone marrow harvested from the indicated treatment groups. (n = 3 biologically independent animals).

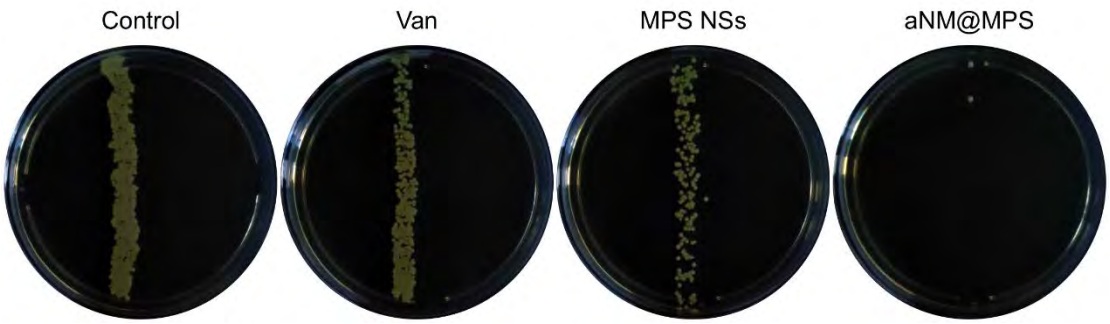

Figure S17 The bacterial colonies of rolling plate assays from the implant in the bone tissues after different treatments (n = 3 biologically independent animals per group).

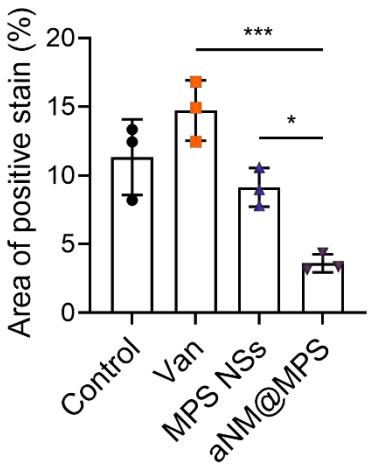

Figure S18. Quantitative analysis of positive stained cells/areas of IL-10. Data are the mean ± s.d. ($n = 3$ biologically independent animals per group). Statistical significance was determined by one-way ANOVA with Tukey's post hoc test. *$P < 0.05$, ***$P < 0.001$.

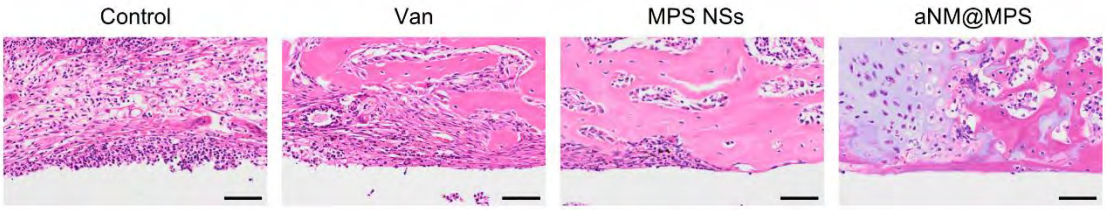

Figure S19. H&E staining of infected peri-implant bone tissues at the study endpoint. Scale bar, 100 μm. (n = 3 biologically independent animals).

Table S1. List of primers used for qRT-PCR

TNF-α	Forward	5’-GTTCCCAAATGGCCTCCC-3’
	Reverse	5’-GTGCTCCTCACCCACACCG-3’
IL-10	Forward	5’-CCCTTTGCTATGGTGTCCT-3’
	Reverse	5’-GTGGCCAGTTTGTTATTTAT-3’
IFN-β	Forward	5’-CAGCTCCAAGAAAGGACGAAC-3’
	Reverse	5’-GGCAGTGTAACTCTTCTGCAT-3’
cGAS	Forward	5’-GTCGGAGTTCAAAGGTGTGGA-3’
	Reverse	5’-GACTCAGCGGATTTCCTCGTG-3’
STING	Forward	5’-GGTCACCGCTCCAAATATGTAG-3’
	Reverse	5’-CAGTAGTCCAAGTTCGTGCGA-3’
CXCL10	Forward	5’-CCAAGTGCTGCCGTCATTTTC-3’
	Reverse	5’-GGCTCGCAGGGATGATTTCAA-3’
β-actin	Forward	5’-GTGACGTTGACATCCGTAAAGA-3’
	Reverse	5’-GTAACAGTCCGCCTAGAAGCAC-3’